ACADEMIA MILITAR
MILITARY ACADEMY

RMA
Royal Military Academy

Hypervelocity impacts against concrete mixed with ceramic spheres

David Teotónio Póvoa Rodrigues Elias

Dissertation submitted in partial fulfilment of the requirements for the degree of

Master of Science in **Military Engineering**

Adviser: Professor Doutor Hugo Miguel Bento Rebelo

Co-adviser: Lieutenant-Colonel David Lecompte

Examination Committee

Chairperson: Prof. Dr. Paula Manuela Dos Santos Lopes Do Rego Figueiredo

Adviser: Prof. Dr. Hugo Miguel Bento Rebelo

Members of the Committee: Prof. Dr. Filipe Santos

Members of the Committee: Lt. Col Pedro José Da Silva Gonçalves Matias

October 2024

Statement

I declare that this document is an original work of my authorship and that it complies with all the requirements of the Code of Conduct and Good Practices of the Military Academy.

Acknowledgments

To my mother, grandmother and grandfather for the patience they had with me and more importantly, the education and values they transmitted. I'm well aware of the sacrifices you made.

To my advisor, Professor Hugo Rebelo, your guidance, availability and open attitude towards the exchange of ideas were instrumental for the success of this dissertation and for making me consider going further than what I imagined.

To Lieutenant Colonel David Lecompte, my heartfelt gratitude for the reception in Belgium, for providing valuable insight and guidance throughout this project as well as being available to verify my professional and personal needs were met during my stay at the Royal Military Academy.

To Bachir Belkassem, Georgios Kechagiadakis and Cpt Mohamed Benrhouma, I extend my gratefulness for your constant availability to both motivating and helping me. On a professional level, I truly benefited from your suggestions and considerations. On a personal level, I will always remember you finding time to provide kind words towards me.

A very special thank you to Lt Baha Rezgui, for the help, good atmosphere and interesting debates we shared on our office during our 4 months in Brussels.

To the 174 POL and the remaining friends made at the Royal Military Academy, I also thank you for having me and for the memories I cherish.

My greatest thanks to Cap Eng João Conceição for facilitating my participation in this project. His presence during the experimental campaign allied to his continuous assistance were crucial for the development of this dissertation.

I thank Lieutenant Colonel Eng Pedro Matias, for the establish links that make this exchange to the Royal Military Academy possible. This opportunity offered to me had the upmost impact on my professional life.

To the 17/18 and 18/19 FOXTROT class, comrades and friends, I could have not made this path without you. A special thanks to Miguel Chambino, António Lima and Francisco Novais for the support provided.

A sincere thank you to all the team in Centre of Competence for Infrastructure Protection (CCPI), to Cap Eng Matos, to Staff Sargent Eng Oliveira, and to all the present from the Heavy Combat Engineering Company, making the experimental field tests possible.

I extent my appreciation to the civilian companies that were part of this project, *Betão Liz* and *Polyanswer,* your contribution and disposal to help was valuable for the accomplishment of this project.

Abstract

Extreme events, whether natural occurring or manmade can have catastrophic consequences, endangering people. Given the current geopolitical situation, there is a need to better protect structures against these threats, minimizing damage to critical infrastructure and safeguarding human lives. Due to this necessity, the Research, Development, and Innovation Centre of the Military Academy (CINAMIL) funded the "Protection of Infrastructures Subjected to Extreme Actions" (PrISAEx) project, from the Centre of Competence for Infrastructure Protection (CCPI), to better understand this phenomena typology and to study ways to mitigate its effects. Within extreme events, hypervelocity impacts (speeds greater than 2000 m/s or 3000 m/s) must be considered.

Therefore, this dissertation will study the behaviour of concrete when faced with hypervelocity impacts, with the goals of evaluating the protective capabilities of concrete structures with the addition of 3 layers of ceramic spheres. The hypervelocity will be achieved using a shaped charge inspired by the PG-7VM warhead, launched by the RPG-7.

For this purpose, LS-DYNA was used to create axisymmetric numerical models of the shaped charge impacting plain concrete targets, as well as concrete targets with the added ceramic spheres. These models were validated with an experimental campaign where the achieved penetration, affected diameter, entry diameter and loss of volume of the different targets were analysed. Furthermore, it was possible to retrieve liners after opening the targets, which provided additional data regarding the loss of their mass.

For the experimental campaign, 3 types of targets were used: S type targets, filled with plain concrete; E type targets were filled with concrete with 3 layers of ceramic spheres and NN targets have the same composition as E targets with the addition of a non-Newtonian fluid, filling the gaps between the spheres.

With the experimental campaign, it was found that the addition of the spheres resulted in decreasing penetration on target by 0,38% and that combining spheres and non-Newtonian fluid caused a 20% reduction in penetration. Furthermore, it was possible to verify that the available analytical penetration models significantly overestimate penetrations, which makes sense considering the difficulties in translating the behaviour of a brittle and non-homogeneous material.

Keywords: Shaped charge; Hypervelocity; Numerical simulation; Ceramic spheres.

Resumo

Eventos extremos, sejam de origem natural ou humana, podem ter consequências catastróficas, colocando em risco vidas humanas. Dada a atual situação geopolítica, é necessário proteger melhor as estruturas contra estas ameaças, minimizando os danos em infraestruturas críticas e salvaguardando vidas humanas. Devido a esta necessidade, o Centro de Investigação, Desenvolvimento e Inovação da Academia Militar (CINAMIL) financiou o projeto "Proteção de Infraestruturas Sujeitas a Ações Extremas" (PrISAEx), do Centro de Competências para a Proteção de Infraestruturas (CCPI), com o objetivo de compreender melhor esta tipologia de fenómenos e estudar formas de mitigar os seus efeitos. Entre os eventos extremos, devem ser considerados os impactos de hipervelocidade (velocidades superiores a 2000 m/s ou 3000 m/s).

Assim, esta dissertação estudará o comportamento do betão face a impactos de hipervelocidade, com o objetivo de avaliar as capacidades de proteção de estruturas de betão com a adição de 3 camadas de esferas de cerâmica. A hipervelocidade será conseguida utilizando uma carga de efeito dirigido inspirada na ogiva PG-7VM, lançada pelo RPG-7.

Para este fim, o *software* LS-DYNA foi utilizado para criar modelos numéricos axissimétricos da carga de efeito dirigido a impactar alvos de betão simples, bem como alvos de betão com 3 camadas de esferas de cerâmica. Estes modelos foram validados através de uma campanha experimental onde foram analisados a penetração, o diâmetro afetado, o diâmetro de entrada e a perda de volume dos diferentes alvos. Além disso, foi possível recuperar partes do *liner* após a abertura dos alvos, o que forneceu dados adicionais sobre a sua perda de massa.

Para a campanha experimental foram utilizados 3 tipos de alvos. Os alvos do tipo S foram preenchidos com betão simples; os alvos do tipo E foram preenchidos com betão com 3 camadas de esferas de cerâmica e os alvos do tipo NN têm a mesma composição dos alvos do tipo E, com a adição de um fluido não-newtoniano que preenche os espaços entre as esferas.

Com a campanha experimental, verificou-se que a adição das esferas resultou numa diminuição da penetração no alvo em 0,38% e que a combinação de esferas e fluido não-newtoniano causou uma redução de 20% na penetração. Além disso, foi possível confirmar que os modelos analíticos de penetração disponíveis sobrestimam significativamente as penetrações, o que faz sentido, tendo em conta as dificuldades em traduzir o comportamento de um material frágil e não-homogéneo.

Palavras-chave: Carga de efeito dirigido; Hipervelocidade; Simulação numérica; Esferas de cerâmica.

Table of Contents

Table of figures

Table of tables

List of abbreviations and acronyms

2D	Two dimensional
3D	Three dimensional
ALE	Arbitrary Lagrangian Eulerian
CAD	Computer aided design
CCPI	Centro de Competências para a Proteção de Infraestruturas
CD	Charge's diameter
CINAMIL	Centro de Investigação, Desenvolvimento e Inovação da Academia Militar
CNC	Computer numerical control
CSC	Conical shaped charge
CSCM	Continuous surface cap model
EOD	Explosive Ordnance Disposal
EOS	Equation of state
FEM	Finite element method
FOI	Swedish Defence Research Agency
HEAT	High explosive anti-tank
HSC	Hypervelocity shaped charge
JH2	Johnson-Holmquist ceramics model
JWL	Jones-Wilkins-Lee
KCC	Karagozian and Case Concrete
LSTC	Livermore Software Technology Corporation
NASA	National Aeronautics and Space Administration
PER	Pugh, Eichelburger and Rostoker
PrISAEx	Proteção de Infraestruturas Sujeitas a Ações Extremas
PVC	Polyvinyl chloride
RHT	Riedel-Hiermaier Thomas
RPG	Rocket propelled grenade
SD	Standard deviation
S.O.	Standoff
UHPC	Ultra-high performance concrete
UHSC	Ultra-high strength concrete

Nomenclature

Latin nomenclature

C	Charge weight
D	Explosive detonation velocity
E	Specific explosive kinetic energy
f_C'	Concrete compressive strength
h	Charge height
K	Tungsten slab thickness
k_1	Jet length coefficient
k_2	Target material coefficient
l	Jet length
M	Initial mass of the liner
n	Geometric configuration constant
P	Penetration depth
v	Jet velocity
v_0	Initial velocity of the projectile
V_D	Velocity of a segment projected at the axis
V_j	Jet element velocity
V_s	Slug element velocity
Y	Material strength

Greek nomenclature

α	Empirical constant for Pack and Evans
β	Angle between the liner wall flowing into the stagnation point and the cone axis
ε	Strain
Θ	Liner angle
λ	Jet consistency constant
ρ_j	Jet density
ρ_t	Target density
σ	Stress
τ	Liner thickness
φ	Bending angle
Φ	Warhead calibre in mm

1. Introduction

1.1 Context and problem definition

It is known that humans have a set of basic needs. The National Aeronautics and Space Administration (NASA) states that we must have food, water, air, and shelter to survive. If any one of these basic needs is not met, then humans cannot survive (Human Needs Exploration: Then and Now Background Information, n.d.). Throughout history, humans have constantly improved their living spaces, seeking better protection from the elements and better ways to ensure their safety from predators or humans. Therefore, construction has always been vital to people, as it is a key part in their defence. That being said, in order to protect people, we must understand what threatens structures and how to protect them.

Extreme events, both natural and manmade, can have catastrophic consequences. For this reason, in 2022, the Research, Development, and Innovation Centre of the Military Academy (CINAMIL) funded the "Protection of Infrastructures Subjected to Extreme Actions" (PrISAEx) project, from the Centre of Competence for Infrastructure Protection (CCPI), to better understand this phenomena typology and to study ways to mitigate its effects. Within extreme events, explosions and hypervelocity impacts must be considered due to the current geopolitical context, with terrorism, wars and increased tensions threatening societies. The Geneva Academy declares that, at the time of writing, there are more than 110 armed conflicts. In some of this conflicts, high-explosive anti-tank (HEAT) warheads are being used not only against armour targets but buildings as well. The high effectiveness of HEAT warheads results from the presence of shaped charges in their design (Żochowski et al., 2021).

Technology accessibility, high production cost and training requirements results in having less modern and advanced HEAT warheads commonly available, which means they present a lower risk when comparing to older and simpler models. Hence, this makes the rocket propelled grenade (RPG) series of antitank projectors, the most widely used shoulder-fired antitank weapons in the world, being used by armies, militias, insurgents and terrorists (Rottman, 2011). Żochowski et al. (2021) mentions that the RPG-7, seen in Figure 1.1, is still being produced by countries like Russia, China, Egypt and Pakistan and being actively used by 90 national armed forces as well as other organizations. For this reason, the PG-7VM warhead, launched by the RPG-7, was the inspiration when designing the shaped charge for this study.

Figure 1.1: RPG being used (Candlin, 2024).

Historically, shaped charges have been used in non-military industries for drilling and destroying obstacles as fast as possible. They are also used with military applications, against safe structures, military vehicles, and different armours (Mehmannavaz et al., 2021). Shaped charges development can be traced back to 1792 when Franz von Baader, mining engineer, remarked that by forming a hollow in a charge, the energy of an explosive blast can be directed to a small area. Then in 1799, von Baader observed that if depressions or shapes were cut in an explosive and placed face down on a steel plate, these shapes would appear on the plate after the detonation took place. This is known as explosive engraving. The influence of the hollow cavity was further studied on the XIX century, first in 1883 by von Foerster and then by Charles E. Munroe in 1888.

Currently, the development and study of shaped charges is still ongoing since there is a constant need to refine them with the introduction of new materials and geometries such as the work of Xu et al. (2019) regarding hypervelocity shaped charges. Hypervelocity impacts refer to a collision that occurs at a speed greater than 2 km/s or 3 km/s, depending on the different metal materials being impacted (Signetti et al., 2022). One way to achieve such velocity is by using shaped charges.

Due to its structural capacity and cost effectiveness, concrete is the most commonly used construction material, including in protective structural components and critical infrastructure (Esteban et al., 2015), as a result, there is a need to obtain knowledge that leads to the implementation of protective measures in concrete structures from the dangers presented by shaped charges. Concrete and the beginning of its use can be traced back to the Romans but gained bigger expression in construction during the XIX century (Calder, 2013). Through the years, research with this material led to development of different types of concrete. A categorization to be made concerns to its compressive strength, in which concrete can be divided into normal strength ($f_C' \leq 50\ MPa$), high strength ($f_C' \leq 120\ MPa$) and ultra-hight strength ($f_C' > 120\ MPa$).

Current studies evaluating shaped charges interaction with concrete targets can be seen gauging their effects on concrete piles (Xue et al., 2022) and testing the influence of different configurations of the shaped charge in penetration (Zhang et al., 2022). Further studies assess the response of ultra-high performance concrete (UHPC) to the charges jet (Resnyansky & Weckert, 2009) or penetration into layered and spaced targets such as the work of Wang et al. (2018). Other studies focus on the addition of different materials to enhance concretes behaviour when faced with impacts, such as steel-fibre concrete in Xiao et al. (2020) and ceramics that will be addressed in Chapter 2.3.

1.2 Motivation and objectives

The previous problem description also gives some insights into the motivation for this dissertation, namely the current geopolitical events that cannot be ignored.

The understanding of explosives and how to optimize them was an early interest of the author since joining the Academy. Shaped charges, due to the complexity of the topic, presented itself as a personal challenge and the feeling of being able to obtain knowledge about such intricate phenomena was a major driving force. It was also valuable to be inserted in a research and development project. To understand some of its development, the continuity within different works and the feeling that this dissertation would hopefully result in adding useful expertise for the Portuguese Army was a major motivation source.

Therefore, this work will focus on evaluating the protective capabilities of concrete structures with the addition of 3 layers of ceramic spheres against hypervelocity impacts. Additionally, nonlinear numerical models will be developed in the present work, which will be validated through an experimental campaign. For the present study, the hypervelocity will be achieved by means of a specially designed shaped charge, inspired by the PG-7VM.

1.3 Dissertation outline

The present subsection describes the organization of the dissertation:

- **Chapter 1, Introduction:** this chapter covers the motivation and objectives of the work to be carried out;
- **Chapter 2, Literature review:** This chapter aims to cover all the relevant state-of-the-art on shaped charges, the behaviour of concrete against impacts, ceramics' uses, as well as a brief overview regarding non-Newtonian fluids. Additionally different analytical, numerical and experimental models will be covered;
- **Chapter 3, Numerical model:** This chapter aims to expose the development of the numerical model and the first decisions made based on it. It will also provide the first results from said models;
- **Chapter 4, Experimental campaign:** This chapter discusses the entire experimental campaign, as well as illustrating its results;
- **Chapter 5, Numerical model improvements:** This chapter introduces the numerical model's improvements implemented based on the experimental campaign's findings;
- **Chapter 6, Conclusions:** The aim of this chapter is to draw conclusions from the work carried out, as well as providing proposals for future work.

2. Literature review

The present chapter aims at providing insights on shaped charges' state-of-the-art, the behaviour of concrete against impacts, ceramic applications, a brief overview regarding non-Newtonian fluids, and the different analytical, numerical and experimental models found to be used regarding hypervelocity impacts.

2.1 Shaped charges

A shaped charge consists of a cylinder of explosive with a conical cavity lined with a thin layer of metal at one end and a detonator at the opposite end (Wang et al., 2008). The charge works by explosively collapsing the liner, which forms a high-velocity jet that will impact the target, see Figure 2.1. As illustrated in Figure 2.2, this jet can reach velocities up to 6-10 km/s at the tip and 1-3 km/s at the tail (Cooper, 1996).

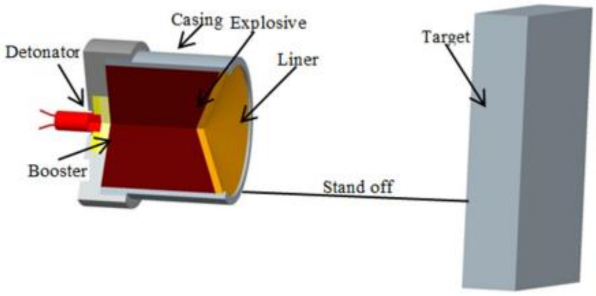

Figure 2.1: Shaped charge composition (Naeem et al., 2019).

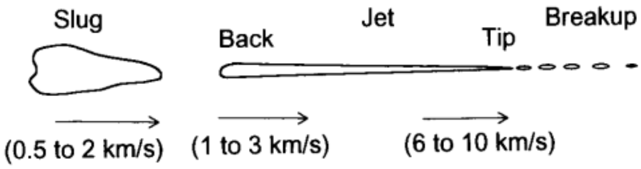

Figure 2.2: Jet velocity gradient (Cooper, 1996).

The hollow cavity, placed at the opposite end of the detonator, causes the gaseous products, formed from the initiation of the explosive, to focus the energy of the detonation products. The focusing of the detonation products creates an intense localized force that, when directed against a metal plate, is capable of creating a deeper cavity than a cylinder of explosive without a hollow cavity, even though more explosive is available in the latter case. This phenomenon is known in the U. S. and Britain as the Munroe effect and in Europe as the von Foerster or Neumann effect (Walters & Zukas, 1989).

Because of the extreme directionality of the energy residing in the jet, it is possible to deliver it to a specific location on a target. The pressure generated in the region of impact has been shown to be so great that the strength of the jet and target materials could be ignored and, therefore, these materials could be treated as perfect fluids (Murphy, 1983). The pressures involved while the collision of the jet with the target were detailed in 1948 by Birkoff, MacDougall, Pugh, and Taylor to be close to a million atmospheres which forced the target material to flow plastically out of the path of the jet.

The key factors to better understand the behaviour of shaped charges are the use of a hollow cavity, the addition of the liner and the subsequent introduction of the standoff. A representation of the above-mentioned key factors and its effects on target can be seen in Figure 2.3.

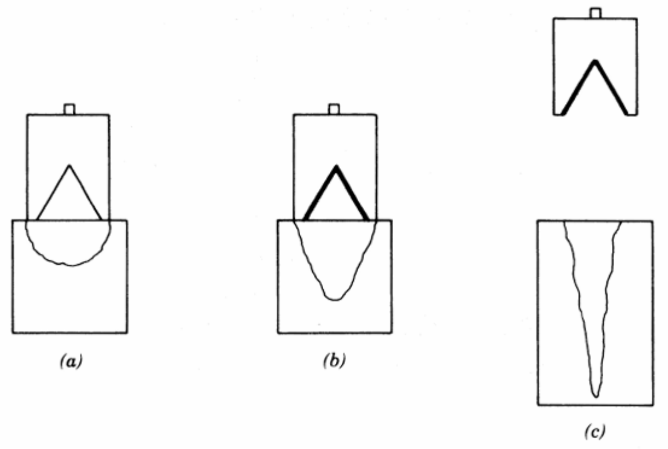

Figure 2.3: Effects on target (Walters & Zukas, 1989).

2.1.1 Standoff

The original von Baader (1792) paper also reports earlier standoff effects when discussing confinement effects on propellants and the positioning of a small air cavity between the explosive powder and the tamping (Walters & Zukas, 1989). It was noted that by having distance between the shaped charge and the target, there was an increase of the effects seen on target (Schardin, 1954).

Cooper (1996) states that at very short standoffs, the jet is still very short and does not have time to form or "stretch". Therefore, the penetration into the target is less than optimal. At very long standoffs, the jet breaks up, and each particle hits further and further off centre and is not contributing to the penetration at the centre of the target. In addition, the jet is rapidly slowed by air resistance in the case of very long standoffs (Austin, 1959).

As a result, it is possible to correlate standoff and achieved penetration, creating a curve in which the highest penetration would be achieved at the optimum standoff. A representation of a general curve for a conical shaped charge was given by Walters & Zukas (1989) and is shown in Figure 2.4. Here it can be seen that the penetration, scaled by the charge's diameter (CD) begins to increase as the scaled standoff (S.O.) becomes larger. However, as previously referred, there's a maximum penetration value that corresponds to a given standoff.

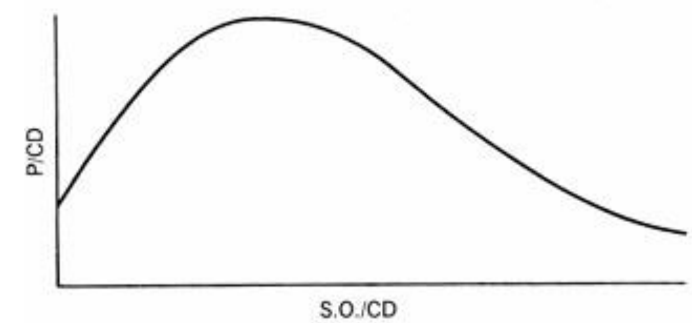

Figure 2.4: Penetration in relation to standoff curve (Walters & Zukas, 1989).

As a general observation, Cooper (1996) also refers that the optimal standoff is between 2 and 6 charge diameters. This general rule can be refined by accessing more recent literature regarding this topic. Kulsirikasem et al. (2011) evaluated the effects of conical shaped charges with different liner materials in steel armour. Resorting to the Finite Element Method (FEM), the authors determined that the optimum standoff distances for copper, tungsten and tantalum are 3.63CD, 3.89CD and 4.46CD, respectively. For concrete targets impacted by an aluminium liner, we can refer to experimental results of penetration versus standoff into high strength heavily reinforced concrete by Murphy et al. (1999). From his results we can see the biggest penetration occurring when the standoff is equal to 4CD.

2.1.2 Parameters that influence shape charges' behaviour

It should be noted that there are multiple parameters that are able to influence the effects of shaped charges. Apart from the influence of the standoff, covered previously, both geometrical and material aspects play a crucial role in the performance of shaped charges. Kulsirikasem et al (2011) summarizes some of the parameters such as liner material, explosive type, as well as the reliability of manufacturing processes. Other factors, namely liner angle and thickness, were also studied by Murphy et al. (2000). For the liner angle, it was observed that, an increase in the liner angle correlated with a reduction in penetration and the growth of the hole diameter. As for liner thickness, the opposite was reported.

However, the most influential factor concerning shaped charges effectiveness was the material used for the liner. Earlier studies conducted with various materials are found in (Kline, 1945), (Schardin, 1954) and (Beeman, 1978), indicating the liner/jet density as the primary factor affecting overall target damage. The fundamental theories of jet penetration show that a higher density jet will penetrate deeper in the target with a smaller borehole diameter, while a lower density jet will penetrate less into the target with a larger borehole diameter (Murphy et al., 1999).

Given its density and price, copper was generally viewed as the material of choice for liners, although others can be used, such has molybdenum, tantalum or tungsten.

2.2 Concrete

To address the mechanical problems of this material, and improve its performance concerning this type of threat, one must first understand its failure mechanisms against impacts. Concrete targets are very vulnerable to shaped charge attacks due to their brittle behaviour and relatively low strength, particularly under tensile loading. The shaped charge jet's impact produces a stress wave in the concrete that reflects at the back surface of the target, generating a tensile wave. Due to the concrete's low tensile strength, failure can easily occur at this location (Resnyansky et al., 2014).

2.2.1 Impacts and failure mechanisms

Kennedy (1976) categorized impacts into two main different types, hard or soft impacts, depending on the projectile deformation. If the impact results in deformation of the target but the deformation of the projectile is insignificant, then this may be considered as a hard impact. However, if there is visible deformation in both projectile and target, then this behaviour must be considered as soft impact (Daudeville & Malécot, 2011).

This terminology was later clarified and summarized into seven phenomena, which were defined in (Li et al., 2005)

- Penetration - combined depth of the spall crater plus the tunnelling depth. Tunnelling depth is the length of the tunnel caused by the projectile into the target;
- Spalling - ejection of target material from the proximal face of the target, represented in Figure 2.5;

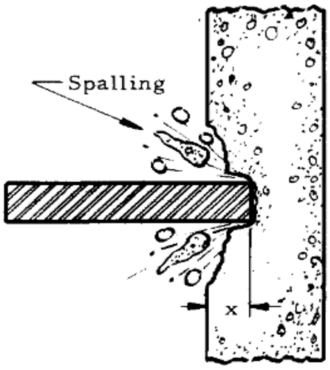

Figure 2.5: Penetration and spalling (Kennedy, 1976).

- Cone cracking - formation of a cone-like crack under the projectile. This phenomenon occurs during the transition phase between penetration and scabbing and is illustrated in Figure 2.6;

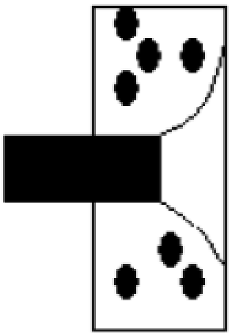

Figure 2.6: Cone cracking (Li et al., 2005).

- Radial cracking - global cracks radiating from the impact point and appearing on either the proximal face, see Figure 2.7(i), the distal face, depicted in Figure 2.7(ii) of the concrete slab or even both faces;

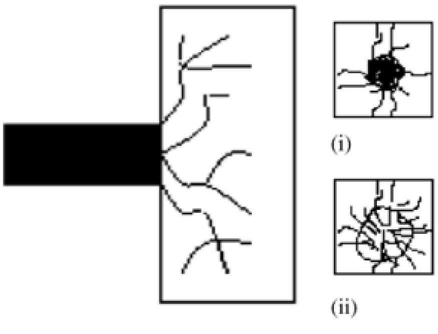

Figure 2.7: Radial cracking (Li et al., 2005).

- Scabbing - ejection of fragments from the distal face of the target. When comparing scabbing and spalling, the zone of scabbing is usually wider than the zone of spalling, but the zone of spalling has greater depth than the scabbing (Latif et al., 2012).
  Scabbing may be visualized in Figure 2.8;

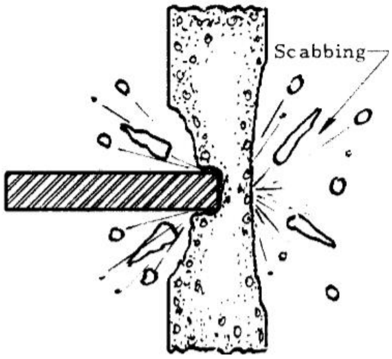

Figure 2.8: Scabbing (Kennedy, 1976).

- Perforation - complete passage of the projectile through the target with or without a residual velocity. The representation of this is provided in Figure 2.9;

Figure 2.9: Perforation (Kennedy, 1976).

- Overall structural responses and failures – are characterized by global bending, shear and membrane responses as well as their induced failures throughout the target, as illustrated in Figure 2.10;

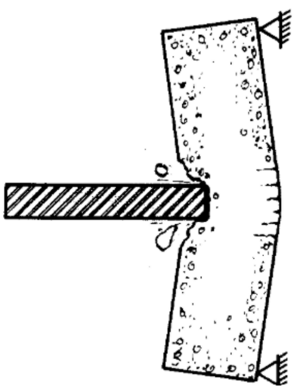

Figure 2.10: Overall structural response (Kennedy, 1976).

Penetration regimes for projectile impacts can also be defined according to the initial velocity of said projectile (v_0). This division can be made into three main groups, from subsonic to hypervelocity:

- Non-deformable regime (v_0 < 10^3 m/s) – the projectile has negligible deformation and conventional mechanical parameters of target, such as strength, stiffness, hardness, and toughness, govern the extent of the penetration (Chen & Li, 2004);
- Semi-hydrodynamic regime (10^3 m/s < v_0 < 3×10^3 m/s) – Alekseevskii in 1966 and Tate in 1967 propose a model for long-rod penetration into a thick target with erosion of the projectile as it penetrates the target. The impact velocity for the validity of the Alekseevskii – Tate model depend on the target and projectile material properties (Chen & Li, 2004);
- Hydrodynamic regime (v_0 > 3×10^3 m/s) – first contemplated for the study of Monroe jets by Birkoff in 1948 and Pack and Evans in 1950 considers that the strengths of projectile and target materials are negligible (Tate, 1967). Therefore, material can be considered as fluids.

2.3 Ceramic

Ceramic materials have been applied as a protective measure against high-velocity impacts for the past years (Asenov et al., 2013). Their use as armour dates to 1970 and is due to their physical and mechanical properties, such as high compressive strength, high hardness, allied to their inexpensive cost (Reddy et al., 2019). The use of advanced ceramics for armour systems allows the defeating of the projectile and ballistic impact energy dissipation providing adequate ballistic protection (Medvedovski, 2010).

The most commonly used ballistic ceramics are alumina (Al_2O_3), silicon carbide (SiC), and boron carbide (B_4C). Among advanced ceramics, alumina has the best cost-benefit ratio. Silicon carbide has a higher cost than alumina, but it is more attractive when considering its lower density and improved mechanical properties. Boron carbide has the highest cost among the three materials; however, it presents the lowest density and the best mechanical properties (Dresch et al., 2021).

Advanced ceramics can also be referred to as the high-performance ceramics, high-tech ceramics, engineering ceramics, fine ceramics, and technical ceramics. They are composed of crystalline material and their specific attributes arise from their controlled composition and manufacturing with detailed regulation (Ayode Otitoju et al., 2020)

Alumina is perhaps the first advanced ceramics. Zhang et al (2008) consider it one of the most important structural ceramics due to its remarkable hardness, strong oxidation resistance, high melting temperature, and high compressive strength. These characteristics, allied with its availability and low cost, result in several studies performed, as stated by Andraskar et al. (2022). Examples of penetration resistance of this material or its use in composite armour, when coupled with metal, can be seen in Lee & Yoo (2001), Gonçalves et al (2004) or Madhu et al (2005), while new composites for enhanced ceramic armour can be found in Shevchenko et al (2024). The application of this material was also studied for concrete protection applications, notably in Tawadrous et al. (2016), and Shao et al. (2019).

Tawadrous et al. (2016) performed numerical simulations for concrete targets being impacted with a steel projectile traveling at 960 m/s, where targets were composed of plain concrete and plain concrete with the addition of a ceramic plate, as demonstrated in Figure 2.11 (i) and (ii), respectively.

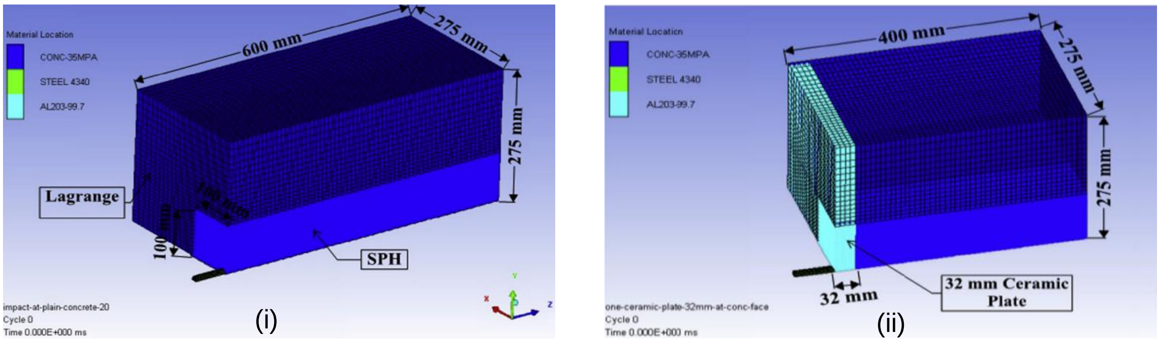

Figure 2.11: Targets composition (Tawadrous et al., 2016).

The main findings made by Tawadrous et al. (2016) show that an existing concrete structure may be strengthened by adding ceramic plates on the concrete face, with an improvement in the penetration resistance of about 66%, as seen in Figure 2.12.

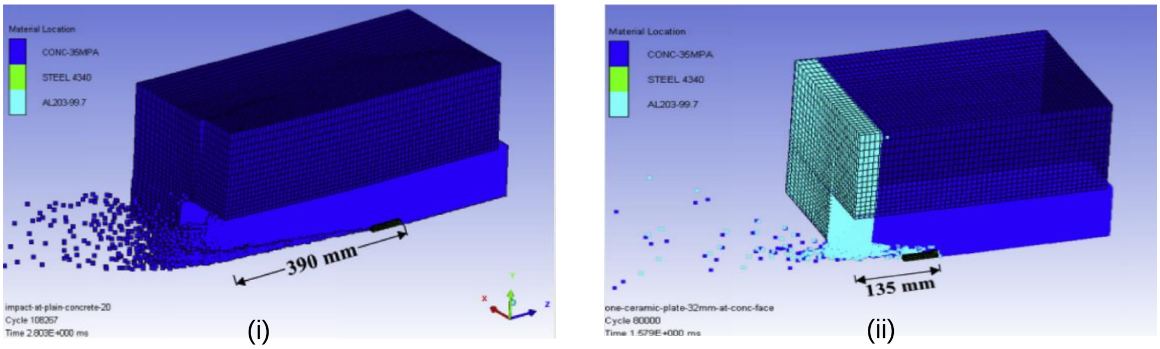

Figure 2.12: Targets penetration (Tawadrous et al., 2016).

High-speed steel projectile impact tests were conducted by Shao et al. (2019), at striking velocities of 545 m/s, 679 m/s, and 809 m/s to investigate the penetration resistance capability of ceramic balls protecting ultra-high strength concrete (UHSC). Additionally, numerical studies were carried out to replicate the projectile penetration, using LS-DYNA. The target dimensions for this experiment are shown in Figure 2.13.

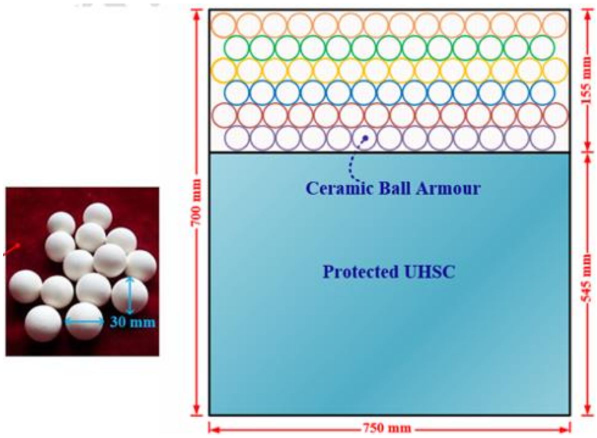

Figure 2.13:Ceramic spheres and target section (Shao et al., 2019).

The results showed that the hex-pack arranged ceramic balls with smaller diameter had better effect in resisting the projectile impact and the employment of ceramic balls in the protective structures is both economical and effective, since the undamaged ceramic balls could be reused and only a small portion of ceramic balls were destroyed (Shao et al., 2019).

After being hit, the rearranged intact ceramic balls, combined with accumulated ceramic fragments, were able to resist the penetration and destruction from multiple batches of impact loads, without the need to replace the protective structure.

2.4 Non-Newtonian fluid

Newtonian fluids demonstrate that, at constant temperature and pressure, for simple shear, the shear stress is proportional to the rate of shear, with the constant of proportionality being the dynamic viscosity. Fluids that don’t conform to this behaviour are known as non-Newtonian, non-linear, complex or rheologically complex fluids (Deshpande et al., 2010).

Non-Newtonian fluids can be categorized according to their behaviour into time-independent and time dependent behaviour. Time-independent behaviour is characterized by the fact that the current value of the rate of shear at a point in the fluid is determined only by the corresponding current value of the shear stress and vice versa (Deshpande et al., 2010). This behaviour can be subdivided into:

- Shear-thinning or pseudoplastic behaviour;
- Visco-plastic behaviour with or without shear-thinning behaviour;
- Shear-thickening or dilatant behaviour.

Time-dependent behaviour means viscosities are not only functions of the applied shear stress or the shear rate but also of the duration for which the fluid has been subjected to shearing as well as their previous kinematic histories. A subsequent subdivision of this can be made into two types of behaviour, thixotropy and rheopexy (or negative thixotropy).

The study of impacts on fluids should be divided taking into consideration the amount of existing fluid. That being said, this topic is separated into impacts facing a large body of fluid, covered by Moghisi et al. (1981), Akers et al. (2006) and de Goede et al. (2019); whereas impacts on a thin layer of fluid can be seen in (Ardekani et al., 2009), (Moss et al., 2011), (Uddin et al., 2012) and (Veltkamp et al., 2022).

2.5 Model typologies

The effects caused by shaped charges may be studied with the use of models either full models or scaled, analytical, or numerical. The overall process, from explosive detonation to total target penetration, occurs in under one-half of a millisecond (for short standoffs). Due to the extremely high pressures, short time durations, and generally harsh environment that exists in the jet/target interaction region, this is an exceedingly complex phenomena to describe analytically and diagnose experimentally (Murphy, 1983). The construction of physical models poses the opportunity to conduct experiments, visualize and compare different effects but it can be challenging. Regarding full scaled models, Dhanasekaran et al. (2017) refer that its testing is difficult and costly for these types of high strain loads.

Therefore, the authors suggest that structural designers should rely on the responses predicted by numerical analysis to design structures against shaped charges.

With the advancement of the computational capabilities, it is now possible to carry out high fidelity simulations of the complex responses of concrete structures subjected to severe shock and impact loads, such as those generated by an explosion and resulting from the impact of a shaped charge's jet. A reliable simulation of the detailed response can play a significant role in the understanding of the physical mechanisms and the development of practical design guidelines based on parametric investigations using validated computational models (Tu & Lu, 2009).

2.5.1 Analytical models

Regarding shaped charges, the development of analytical models revolves around liner collapse and jet formation or the target penetration estimation.

2.5.1.1 Liner collapse

The collapse of the liner and the jets velocity gradient was first detailed in 1952 by Pugh, Eichelburger and Rostoker with the PER theory. According to the authors, the original position of the liner elements affects its collapse velocities, decreasing them continuously from apex (which is the liner portion closest to the detonator), to the base (the furthers portion of the liner in relation to the detonator).

The rate of decrease is very gradual near the apex but becomes much more rapid near the base. This is just what one should expect, since near the base the belt of explosive surrounding the liner is much thinner and the masses of the liner elements are much greater than near the apex. The velocity of the jet and the proportion of the liner that goes into the jet are significantly influenced by the angle that the collapsing liner makes with the shaped charge's axis. As the angle increases the velocity of the jet decreases, but the proportion of the liner going into the jet increases (Pugh et al., 1952). A representation of the liner collapse is provided by Figure 2.14.

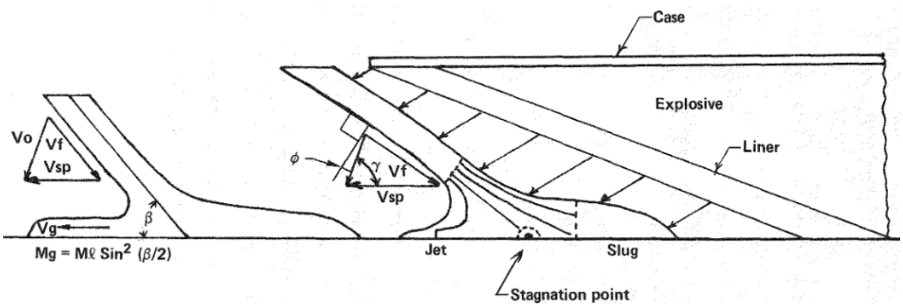

Figure 2.14: Liner collapse representation (Murphy, 1983).

The jets' velocity may be described analytically by the following equation:

$$V_D = 2D\ sin\ \frac{\varphi}{2} \tag{2.1}$$

- V_D – velocity of a segment projected at the axis
- D – explosive detonation velocity
- φ - bending angle

The projected segments of liner will be divided into jet and slug elements, represented by the respective equations:

$$V_j = V_0(\csc\frac{\beta}{2})\cos(\Theta + \varphi - \frac{\beta}{2}) \tag{2.2}$$

$$V_s = V_0(\sec\frac{\beta}{2})\sin(\Theta + \varphi - \frac{\beta}{2}) \tag{2.3}$$

To estimate V_0, one can also apply other analytical approaches such as the Gurney velocity approximation and extensions to this method. This approximation is frequently used to estimate the velocity attained by a metal in contact with a detonating explosive, with different equations available for symmetric and asymmetric configurations.

The usefulness of the Gurney formulas, in application to one-dimensional computer codes for shaped charge design, has called for their extension to predict the velocities of imploding cylinders. Two different approaches by Chou, Carleone, and Flis in 1981 and by Chanteret in 1983 have led to improvements which were shown to predict correctly two-dimensional code simulations for unconfined charges (Hirsch, 1986).

Chou, Carleone, and Flis (1981) provide a popular expression for a single flat plate backed by a slab of explosive, used for shaped charge studies, that can be simplified by:

$$V_0 = \sqrt{2E}\left[\frac{3}{\left(4\cdot\frac{M}{C}\right)^2 + 5\cdot\frac{M}{C} + 1}\right]^{\frac{1}{2}} \tag{2.4}$$

- M: initial mass of the liner
- C: charge weight
- E: specific explosive kinetic energy

It should be pointed that the parameter $\sqrt{2E}$ is also known as Gurney constant or Gurney characteristic velocity. Alternatively, Chanteret developed an analytical model for symmetrical geometries. This velocity equation is available in (Kennedy, 1998) and is expressed as follows:

$$V_0 = \sqrt{2E_G}\left[\frac{M}{C} + \frac{n}{n+2}\right]^{\frac{-1}{2}} \tag{2.5}$$

The use of E_G rather than E is because it is a function of gas expansion. The constant n depends on the geometric configuration ($n = 1$ for symmetrical plane sandwiches, and $n = 2$ for cylinders with a constant wall thickness).

2.5.1.2 Penetration

To estimate penetration depths, there was a need to develop models influenced by both theoretical studies and experimental research. Existing theories for penetration of shaped charge jets into homogeneous targets are extensive and well substantiated. For concrete targets, however, their application has not been shown. The basic hydrodynamic theory has not been experimentally verified for inhomogeneous, compressible, brittle materials with low strength (Murphy, 1983).

Birkhoff et al. (1948) developed a simple model to determine the penetration depth resulting from a hypervelocity jet impact, defined in equation 2.6,

$$P = l \cdot \sqrt{\frac{\rho_j}{\rho_t}} \tag{2.6}$$

where P is the penetration depth, l is the jet length, ρ_j is the jet density and ρ_t is the target density.

This simplified model utilizes 3 main assumptions.

- Both jet and target behave like ideal liquids;
- The jet has a constant and uniform speed;
- The jet has the shape of a rod.

This model was refined by the introduction of an extra coefficient λ, where $1 < \lambda < 2$:

$$P = l \cdot \sqrt{\frac{\lambda \cdot \rho_j}{\rho_t}} \tag{2.7}$$

λ is a constant that equals one for a continuous jet and two for a particulated jet and ρ_j is now the average jet density, taking into consideration the gaps between particles (Walters et al., 1988).

A more thorough model was proposed by Pack and Evans (1950) that acknowledges a reduction in penetration due to the strength of the target material. This reduction factor is a function of the empirical constant α, the material strength Y and the jet velocity v. Equation 2.8 reproduces the proposed model.

$$P = l \cdot \sqrt{\frac{\rho_j}{\rho_t}} \cdot \left(1 - \frac{\alpha Y}{\rho_j \cdot v^2}\right) \tag{2.8}$$

The Swedish Design Manual for Protective Construction, FKR2011, provides a formula regarding shaped charge calculation models for explosive ordnance disposal (EOD) operations. This formula developed by the Swedish Defence Research Agency (FOI) is intended for practical applications (Elfving et al., 2005). The following expression may be used to attain an estimation on the penetration into fortifications:

$$P = \Phi \cdot k_1 \cdot k_2 \cdot \sqrt{\frac{\rho_j}{\rho_t}} \tag{2.9}$$

- P – depth of penetration in mm;
- Φ – warhead calibre in mm;
- k_1 – coefficient for jet length taken from Table 2.1;

Table 2.1: k_1 values for length coefficient.

Warhead	Calibre (mm)	k_1
Sub-munition	< 70	8
Hand-held anti-tank weapon	< 110	8/12/16*
Light anti-tank missiles	< 130	12/16**
Heavy anti-tank missiles	< 180	12/16**
Ballistic missiles	< 350	12/16**
*k_1 = 8 is used only for older ammunition with a depth of penetration into steel up to 4 diameters, else k_1 = 12. ** k_1 = 12 is used for all munitions, except late versions, with a depth of penetration into steel corresponding to 8 calibres.		

- k_2 – coefficient for target material taken from Table 2.2;

Table 2.2: k_2 values for target coefficient.

Target material	Density (kg/m^3)	k_2
Sand, gravel	1600	1,0
Ordinary concrete (C40)	2400	0,8
High-strength concrete (C140)	2500	0,5

The information needed to use equation 2.9 is in most cases available through ammunition databases. However, it does not account for standoff influence which should be considered in order to avoid overly conservative values for penetration (Johnsson et al., 2012). This leads to the introduction of the reduction factor shown by the following expression:

$$k_{\text{distance}} = \frac{1}{1 + \left(\frac{\text{S.O.} - 7\Phi}{14\text{S.O.}}\right)} \tag{2.10}$$

The final expression, taking this reduction factor into account follows:

$$P = \Phi \cdot k_1 \cdot k_2 \cdot k_{\text{distance}} \cdot \sqrt{\frac{\rho_j}{\rho_t}} \tag{2.11}$$

2.5.2 Numerical analysis

Finite element analysis provides the most detailed information for impact events caused by shaped charges. This is frequently made by using different software, nonetheless, a literature review reveals that the most commonly used commercial software are LS-DYNA, AUTODYN and ABAQUS.

Due to the availability of the commercial software, the focus of this subsection will be models built using LS-DYNA. This software was developed by Livermore Software Technology Corporation (LSTC). Downes et al. (2016) refer that LS-DYNA is an explicit, nonlinear finite element code widely used by the defence and aerospace industry to simulate dynamic impacts, such as blast and bird strike events. Features of this code include large material and element libraries, various contact algorithms and a high level of accuracy.

There are two main topics that should be considered when discussing finite element models. The number of dimensions and the formulation used to build the model. The two-dimensional (2D) approach was deemed the most recurrent, although it is possible to conduct three-dimensional (3D) shaped charge modelling and analysis. The use of 2D can be justified, since this simplification is able to capture the essential behaviour of the charge, giving accurate results, and it has less computational cost when compared with the 3D approach.

When it comes to the formulation used regarding shaped charges modelling, a common methodology found is the Arbitrary Lagrangian Eulerian Method (ALE). With ALE, in its Eulerian formulation, the different materials flow through a mesh that is fixed in space and allows each element to contain a mixture of different materials (Olovsson,2000.). This method may be used to simulate moving fluids interacting with structures and their dynamic response and avoids element distortion.

Malesa et al. (2021) made a 2D ALE shaped charge model with LS-DYNA to study the interaction between the shaped charge and a steel target with different standoffs. Figure 2.15 depicts a scheme of the numerical model.

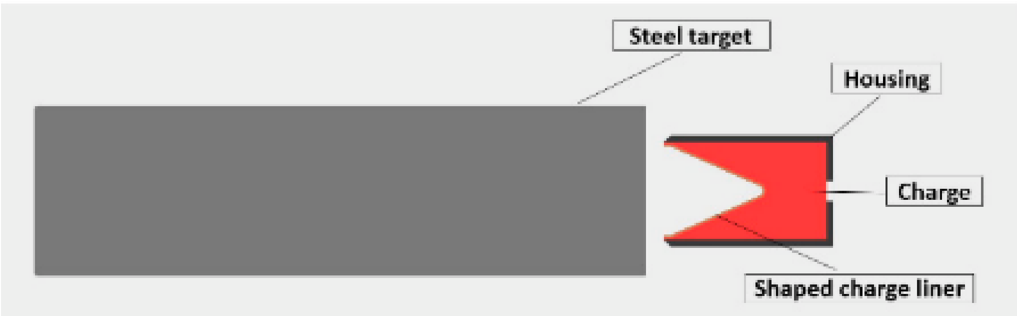

Figure 2.15: 2D ALE model representation (Malesa et al., 2021).

From their results, the influence of the standoff regarding penetration, as well as the different velocity gradients achieved at the different standoffs can be seen. This model was validated with an experimental campaign and the penetration depth obtained by means of numerical analyses and experimental tests were characterized by a difference at the level of 4–8%, which made it possible to consider the used method as effective for modelling the charge.

Figure 2.16 offers a comparison between the penetration process for two different standoff distances while Figure 2.17 illustrates the link between standoff distance and penetration.

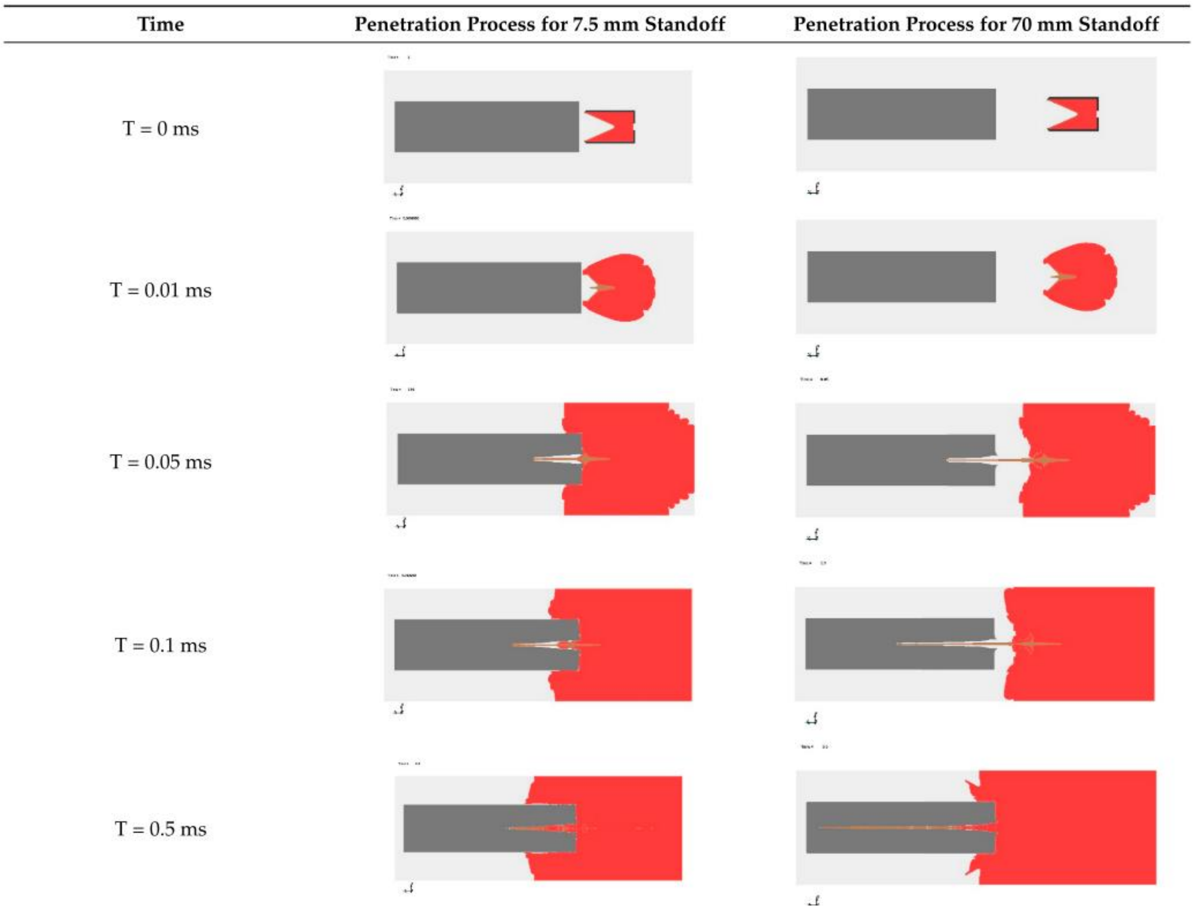

Figure 2.16: Penetration at different standoffs (Malesa et al., 2021).

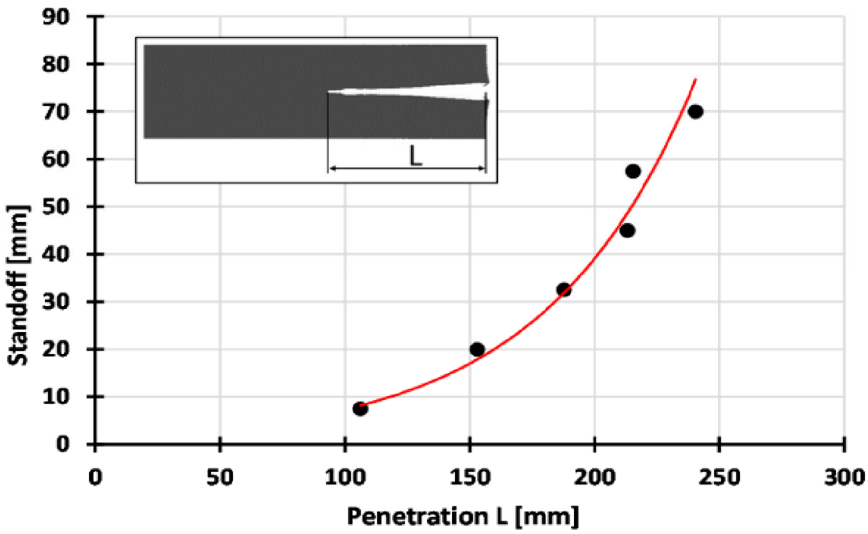

Figure 2.17: Penetration and standoff curve (Malesa et al., 2021).

Resnyansky et al. (2004) provides an early ALE model for interaction between concrete and shaped charge jets. The simulations were done to evaluate the differences on target effect caused by variations in liner angle (θ), charge height (h), liner thickness (τ) and standoff. A comparison of the results achieved with different configurations can be seen in Figure 2.18 to Figure 2.20.

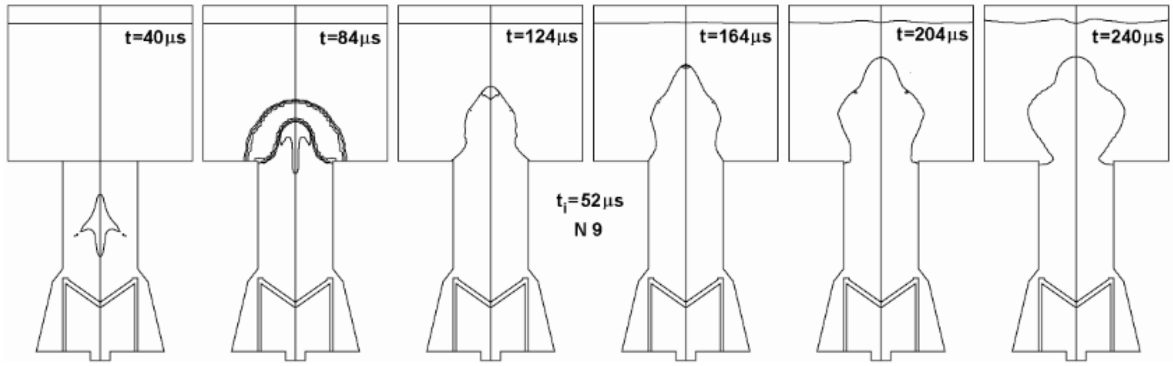

Figure 2.18: Simulation for h=36mm, θ =110˚, τ =5mm, and S.O.=127mm (Resnyansky et al., 2004).

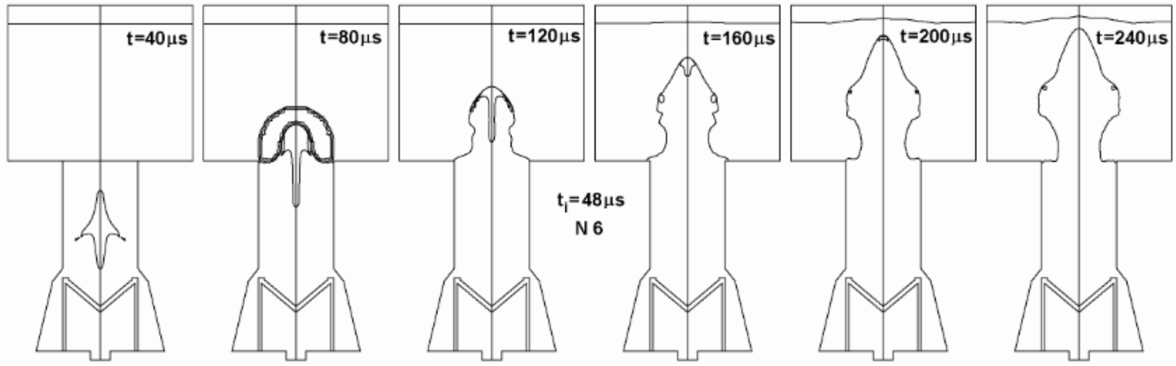

Figure 2.19: Simulation for h=36mm, θ =90˚, τ =5mm, and S.O.=127mm (Resnyansky et al., 2004).

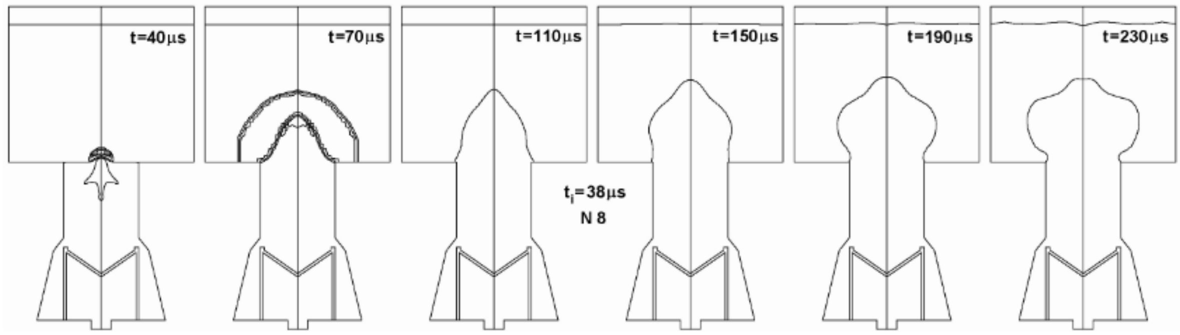

Figure 2.20: Simulation for h=36mm, θ =110˚, τ =3mm, and S.O.=93mm (Resnyansky et al., 2004).

From these simulations, it was possible to determine that a 90˚ liner angle is nearly ideal and that the optimal standoff should be between 70 mm and 100 mm.

2.5.3 Experimental models

Like preciously mentioned, experimental campaigns are costly, therefore, they are mainly used to validate numerical models, which are then used to extract more information or design structures against this threat. Common setups used for shaped charge experiments consist of putting the assembled charge on top of the determined target at a given standoff distance. Such setup can be seen in Resnyansky et al. (2014) and is illustrated in Figure 2.21.

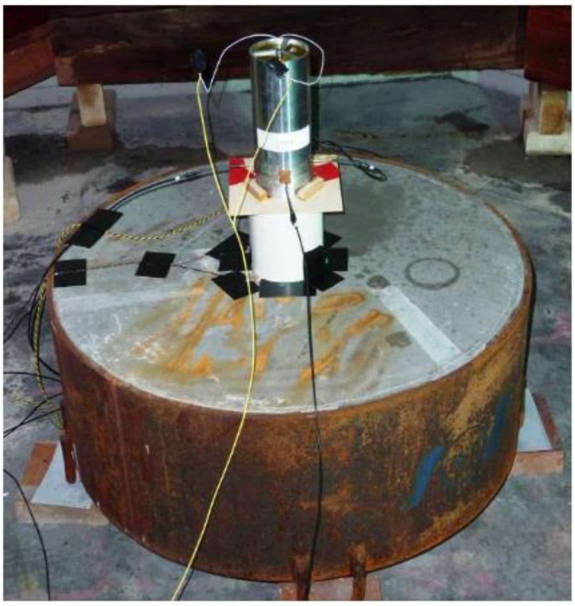

Figure 2.21: Common experimental setup (Resnyansky et al., 2014).

With this setup it was possible to compare UHPC targets and plain concrete targets, measuring penetration, borehole diameter and damage to the front and rear of the target. The damage suffered by the target is depicted in Figure 2.22 and Figure 2.23.

Figure 2.22: UHPC damage to front and rear face (Resnyansky et al., 2014).

Figure 2.23: Plain concrete damage to front and rear face (Resnyansky et al., 2014).

When comparing both materials, it was observed that the plain concrete targets had a bigger depth of penetration as well as a larger borehole diameter, as showed in Figure 2.24.

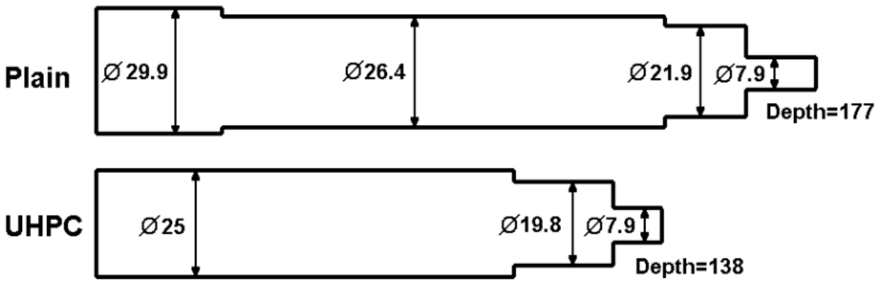

Figure 2.24: Comparing plain and UHPC target damage (Resnyansky et al., 2014).

Other recent example comes from Xu et al. (2020), which compares the behaviour of layered and spaced concrete targets against hypervelocity shaped charges. This study also evaluated the effects of different geometries and compositions for the liner, comparing a conventional conical shaped charge (CSC) with a hypervelocity shaped charge (HSC), as illustrated in Figure 2.25 (a) and (b), respectively.

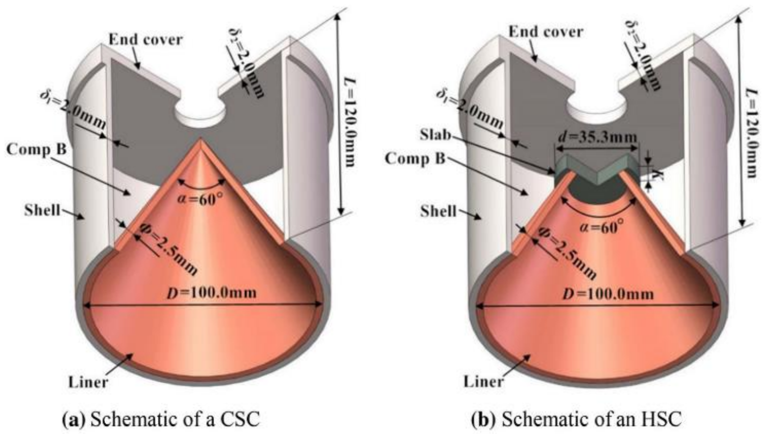

Figure 2.25: Conical and hypervelocity shaped charge (Xu et al., 2020).

In this case, the geometry of the HSC included a tungsten slab, with 2,5 mm; 7,5mm and 10 mm thickness (K), seen in Figure 2.26.

Figure 2.26: HSC tungsten slab thickness (Xu et al., 2020).

The setup used for their experimental campaign is seen in Figure 2.27.

Figure 2.27: Layered and spaced concrete targets (Xu et al., 2020).

Figure 2.28 provides an illustration of the collected data regarding the HSC with 5 mm tungsten slab thickness and the CSC.

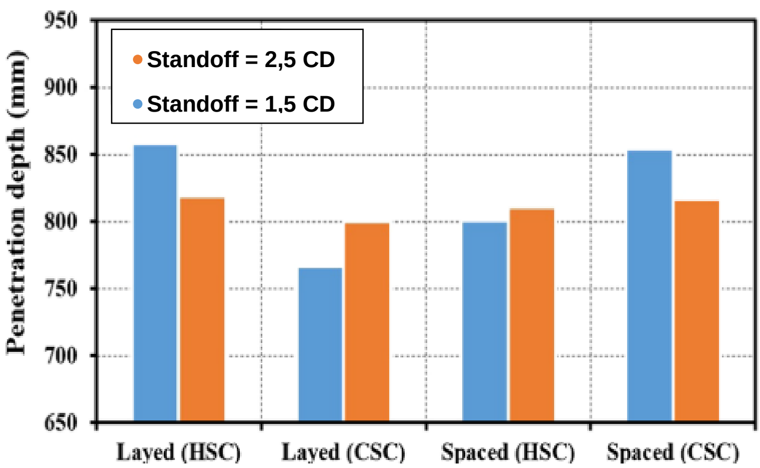

Figure 2.28: Comparison between HSC with K = 5 mm and CSC (Adapted from (Xu et al., 2020)).

It was concluded that, for HSC, higher penetrations in layered targets were achieved at 1,5CD standoff when comparing to 2,5CD standoff. However, the opposite was reported for the CSC, with the 2,5CD standoff achieving higher penetrations than 1,5CD standoff. For spaced targets, HSC performed similar penetrations at both 1,5CD and 2,5CD standoff. This behaviour was not observed for the CSC with the 1,5CD standoff penetrating more than 2,5CD standoff. It was also observed that the achieved penetrations caused by HSC in layered targets was similar to the one performed by CSC on spaced targets. Furthermore, the jet velocity of HSC with K = 7.5 mm was 55.3% faster than that of CSC. The penetration depth of layered targets caused by HSC with K = 7.5 mm increased by 31.3% than that formed by CSC.

3. Numerical model

This chapter presents the development of the numerical models used to determine the interaction between jet and target. The validation of the created numerical models will be done through the analysis of the data collected in the experimental campaign and comparing it against the numerical models' results. This validation will also allow access to data that was not possible to collect during the experimental campaign.

As previously mentioned in subsection 2.5.2, LS-DYNA was used to elaborate the finite element analysis models. The construction of the model itself is done with LS-Prepost, subsequently, the LS-DYNA solver performs the necessary iterations to analyse the numerical model. To visualise the results, LS-Prepost is once again used.

3.1 Consistency units

To operate this software and attain accurate results, a consistent set of units is required. LS-DYNA support provides examples of unit consistency tables, as well as three equations to further understand this topic. These equations are as follows:

$$1 \text{ force unit} = 1 \text{ mass unit} \times 1 \text{ acceleration unit} \quad (3.1)$$

$$1 \text{ acceleration unit} = 1 \text{ length unit} / (1 \text{ time unit})^2 \quad (3.2)$$

$$1 \text{ density unit} = 1 \text{ mass unit} / (1 \text{ length unit})^3 \quad (3.3)$$

The numerical models for this dissertation were created with the unit system shown in Table 3.1.

Table 3.1: Unit consistency.

Length	Time	Mass	Force	Pressure	Energy	Speed	Density
mm	ms	kg	kN	GPa	kN-mm	mm/ms	kg/mm^3

3.2 Construction of the numerical model

3.2.1 Shaped charge geometry

As previously stated, the design of the utilized shaped charges took inspiration on a commonly used RPG warhead, the PG-7VM (see Figure 3.1).

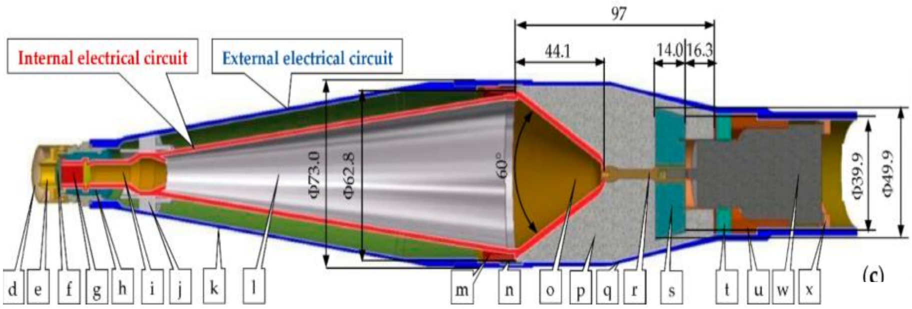

Figure 3.1: PG-7VM warhead (Żochowski et al., 2021).

The final geometry used for both the numerical models and the experimental campaign is depicted in Figure 3.2 and was achieved by taking these measurements into consideration, adapting them.

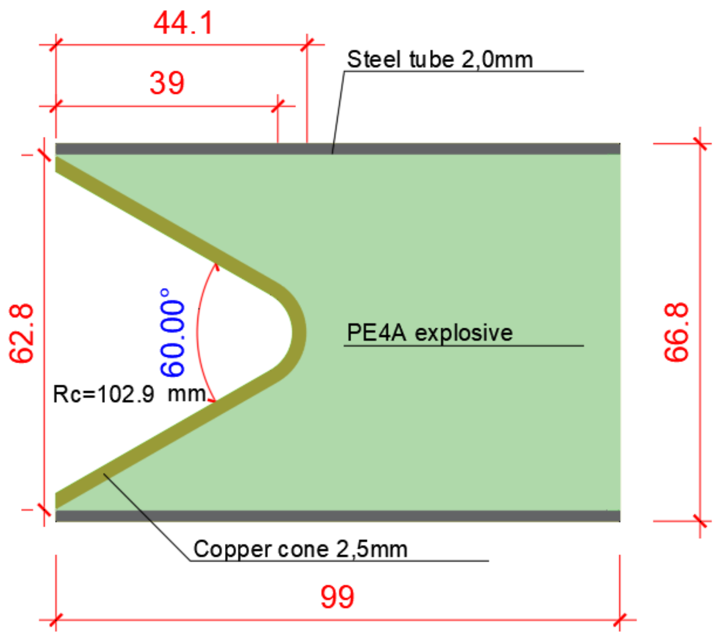

Figure 3.2: Shaped charge geometry in mm.

Based on the envisioned geometry and the project goals, a decision was made to create a 2D ALE axisymmetric model. This choice significantly reduces computational costs, ensuring that a greater number of preliminary models could be run and, with that, enabling better decisions regarding the charge's construction.

Despite providing more accurate results, a finer mesh also requires more computational cost. Therefore, a mesh sensitivity study was conducted, on which preliminary models were constructed using a square mesh size of 0,5 mm and 1 mm. Analysing the attained results, it was possible to conclude that a 1 mm mesh was appropriate for the continuation of this project, since it requires less computational resources and yields similar results when compared with the 0,5 mm mesh.

3.2.2 Material modelling

Since LS-DYNA has different material models available to accurately simulate the behaviour of the shaped charge, there was a need to determine which ones to use for each of the shaped charge's components. The liner is faced with severe conditions involving pressure and materials deformation during detonation and subsequent liner collapse. For that reason, the Johnson-Cook material model was chosen since it is used when the material is subjected to high strain rates and temperatures (Johnson & Cook, 1983). Due to the lack of material parameters available in the literate and in order to reduce computational costs, the simplified version of this material model was used (MAT_SIMPLIFIED_JOHNSON_COOK).

An iterative plane stress update is used for the shell elements, but due to the simplifications related to thermal softening and damage, this model is 50% faster than the full Johnson-Cook implementation. To compensate for the lack of thermal softening, limiting stress values are introduced to keep the stresses within reasonable limits (LSTC, 1992).

The simplified Johnson-Cook yield stress can be expressed as follows:

$$\sigma_y = \left(A + B\varepsilon^{p^n}\right)(1 + C \ln(\varepsilon^*)) \tag{3.4}$$

The variables A, B, C and n represent the yield stress, the hardening coefficient, the strain-rate coefficient and the hardening exponent, respectively. The effective plastic strain corresponds to ε^p and ε^* depicts the normalized effective strain rate. The material parameter values used in the present work to simulate the nonlinear behaviour of copper are shown in Table 3.2 and were taken from Johnson & Cook (1983).

Table 3.2: Copper material parameters.

MAT_SIMPLIFIED_JOHNSON_COOK		
Parameter	**Unit**	**Value**
RO – Mass density	kg/mm^3	$8{,}96 \cdot 10^{-6}$
E – Young's modulus	GPa	117,2
A – Yield stress	GPa	0,090
B – Hardening coefficient	GPa	0,292
n – Hardening exponent	-	0,310
C – Strain-rate coefficient	-	0,025

The steel casings' nonlinear behaviour could also be simulated utilizing the Johnson-Cook model. However, to decrease computational costs and given the less harsh conditions this material is subjected, it was decided to use a different material model. The plastic kinematic material model is a very cost-effective model, formulated by Krieg and Key, that is able to simulate the isotropic and kinematic hardening plasticity with the option of including rate effects (Abedini & Zhang, 2021). It is typically used for modelling steel and other metals (Ranade, 2014). The input parameters used for this material model are exposed in Table 3.3.

Table 3.3: Steel material parameters.

MAT_PLASTIC_KINEMATIC		
Parameter	**Unit**	**Value**
RO – Mass density	kg/mm^3	$7{,}8 \cdot 10^{-6}$
E – Young's modulus	GPa	210
SIGY – Yield stress	GPa	0,275
ETAN – Tangent modulus	-	0
BETA – Hardening parameter	-	0

To address the simulation of high explosives, MAT_HIGH_EXPLOSIVE_BURN material model was used. Nonetheless, this material model requires the use of an equation of state (EOS), therefore, the Jones-Wilkins-Lee (JWL) equation of state was used in combination with the referred material model. The JWL EOS is an empirical mathematical expression based on the Gruneisen equation of state. Its practical nature and the large data base of experimental and popular explosives is an advantage when compared with other equations of state. Despite neglecting factors such as viscosity, conductivity, friction, and gravity (Urtiew & Hayes, 1991), the JWL EOS is commonly used to simulate the detonation of high explosives. The JWL defines the pressure as a function of the relative volume, V, and detonation energy per unit volume, E, (Tabatabaei & Volz, 2012):

$$p = A'\left(1 - \frac{w}{R_1 V^*}\right)\mathrm{e}^{-R_1 V^*} + B'\left(1 - \frac{w}{R_2 V^*}\right)\mathrm{e}^{-R_2 V^*} + \frac{wE}{V^*} \tag{3.5}$$

Where A, B, R_1, R_2 and ω are the materials constants. The corresponding material and EOS parameters of the explosive used are listed in (McIntosh, 2014). Table 3.4 and 3.5 respectively provide the input values for the material model and EOS parameters.

Table 3.4: Explosive material parameters.

MAT_HIGH_EXPLOSIVE_BURN		
Parameter	**Unit**	**Value**
RO – Mass density	kg/mm^3	$1{,}4 \cdot 10^{-6}$
D – Detonation velocity	mm/ms	7000
PCJ – Chapman-Jouget pressure	GPa	25

Table 3.5: Explosive EOS parameters.

EOS_JWL		
Parameter	**Unit**	**Value**
A	GPa	373,8
B	GPa	3,747
R_1	-	4,15
R_2	-	0,9
OMEG	-	0,35
E_0 - Initial internal energy	GPa	0,85

The air was simulated using the NULL material model in combination with the linear polynomial EOS, which is used to consider the air as an ideal gas. The input parameters for the material model and EOS can be seen in (Wu et al., 2007). The material parameters used are given in Table 3.6.

Table 3.6: Air material parameters.

MAT_NULL		
Parameter	**Unit**	**Value**
RO – Mass density	kg/mm^3	$1{,}275 \cdot 10^{-9}$
PC - Pressure cutoff	-	0
MU - Dynamic viscosity	-	0

The linear polynomial equation of state relates pressure P to the energy per unit volume E_0 and is expressed by:

$$P = c_0 + c_1 u + c_2\mu^2 + c_3\mu^3 + (c_4 + c_5\mu + c_6\mu^2)E_0 \tag{3.6}$$

This EOS may be used to model gas with the gamma law equation of state, defining all the polynomial equation coefficients to the value zero, apart from C_4 and C_5 (LSTC, 1992), which are a function of the heat capacity ratio. Table 3.7 offers the EOS parameters used for the air modelling.

Table 3.7: Air EOS parameters.

EOS_LINEAR_POLYNOMIAL		
Parameter	**Unit**	**Value**
C_4	kg/mm^3	0,4
C_5	-	0,4
E_0 - Initial internal energy	-	$2{,}533 \cdot 10^{-4}$
V_0 - Initial relative volume	-	1

LS-DYNA has different concrete constitutive models available to simulate its nonlinear behaviour, such as the continuous surface cap model (CSCM), the Riedel-Hiermaier Thomas model (RHT), the Winfrith model, and the Karagozian & Case concrete model (KCC). The performance of the above constitutive models was evaluated by Dhanasekaran et al. (2017) and Abedini & Zhang (2021). Their work indicates that MAT_072R3, the KCC Model - Release III, was suitable to be used with blast loadings and that this material supports ALE formulations. To use this material model, the user only needs to specify the concrete's unconfined compression strength. This poses a noteworthy advantage in comparison to other models that require more inputs. However, if a dynamic analysis is required, the concrete density must also be provided. Both these variables are illustrated in Table 3.8. The remaining parameters to completely define the material model and EOS are automatically generated (Schwer & Malvar, 2005).

Table 3.8: Concrete material parameters.

MAT_CONCRETE_DAMAGE_REL3		
Parameter	**Unit**	**Value**
RO – Mass density	kg/mm^3	$2{,}4 \cdot 10^{-6}$
A_0 – Maximum shear failure surface parameter	GPa	-0,042

To simulate the ceramic spheres' behaviour, the Johnson-Holmquist ceramics model, also referred as JH2 material model, was used. This model is employed when modelling ceramics, glass and other brittle materials and was developed to address concerns with the first Johnson-Holmquist, JH1, since it did not allow gradual softening and there was self-healing of some fractured materials when using Eulerian codes. JH2 is applicable for brittle materials subjected to high strain rates and high pressures and is well-suited for computations in both Lagrangian and Eulerian codes. The equivalent strength of the material is a function of the intact strength, fractured strength, strain, strain rate, pressure and damage (Johnson & Holmquist, 1994). Further understanding of this constitutive model is provided by Cronin et al. (2003), focusing on its implementation and validation. According to the JH2 material model, the equivalent stress for a ceramic-type material is given by:

$$\sigma^* = \sigma_i^* - D(\sigma_i^* - \sigma_f^*) \tag{3.7}$$

where the damage D is $(0 \leq D \leq 1)$, σ_i^* is the normalized intact equivalent stress and σ_f^* is the normalized fracture stress. The normalized stresses can be respectively defined by:

$$\sigma_i^* = A(P^* + T^*)^N(1 + C\ln(\varepsilon^*)) \quad (3.8)$$

$$\sigma_f^* = B(P^*)^M(1 + C\ln(\varepsilon^*)) \quad (3.9)$$

The used input parameters can be seen on Table 3.9 and were taken from Shao et al. (2019).

Table 3.9: Alumina material parameters.

MAT_JOHNSON_HOLMQUIST_CERAMICS		
Parameter	**Unit**	**Value**
RO – Mass density	kg/mm^3	$3{,}65 \cdot 10^{-6}$
G – Shear modulus	GPa	156
A – Intact normalized strength parameter	-	0,88
B – Fractured normalized strength parameter	-	0,28
C – Strength parameter	-	0,007
M – Fractured strength parameter	-	0,6
N – Intact strength parameter	-	0,64

3.3 Preliminary models

As stated before, the elaboration of the first models was performed to aid in the decision-making process regarding the design of the shaped charge. The two main goals for these models were to determine the necessity of a backplate for the casing and the optimal standoff distance. To achieve said goals, firstly, a numerical model of the shaped charge was developed, see Figure 3.3. Secondly, in order to determine the ideal standoff distance, the numerical model of both the shaped charge and concrete target illustrated in Figure 3.4 was created.

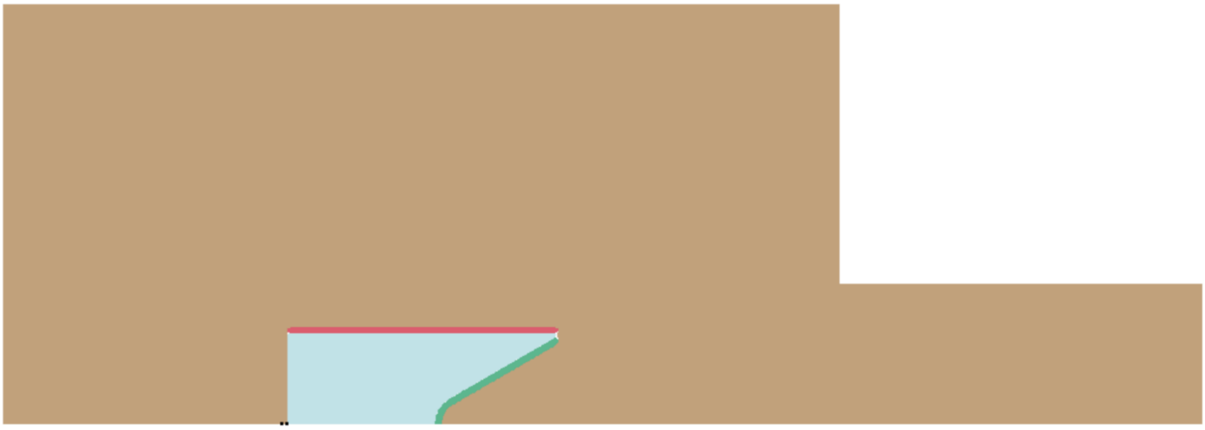

Figure 3.3: Shaped charge FEM.

Figure 3.4: Concrete FEM.

- Air - Explosive - Casing - Liner - Concrete

3.3.1 Casing geometry

The influence of the backplate was studied using the two geometries depicted in Figure 3.5, with (i) being closed back and (ii) being an open back casing. To perform this study, a constant standoff of 240 mm was used, the reason for this distance will be provided in subsection 3.3.2.

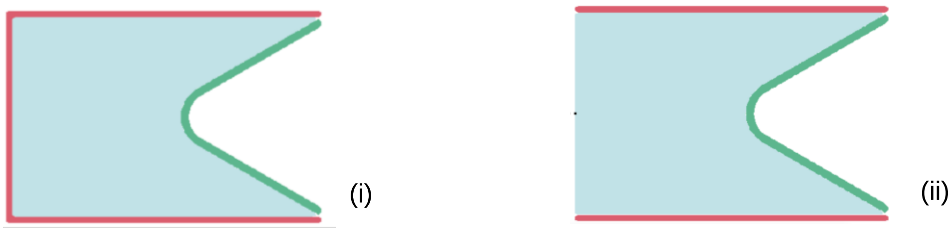

Figure 3.5: Casing geometries.

Figures 3.6 and 3.7 illustrate the achieved penetrations for the above-mentioned geometries. The closed casing geometry achieves a 430 mm penetration, while the open casing attains a 419 mm penetration, representing a 2,56% reduction.

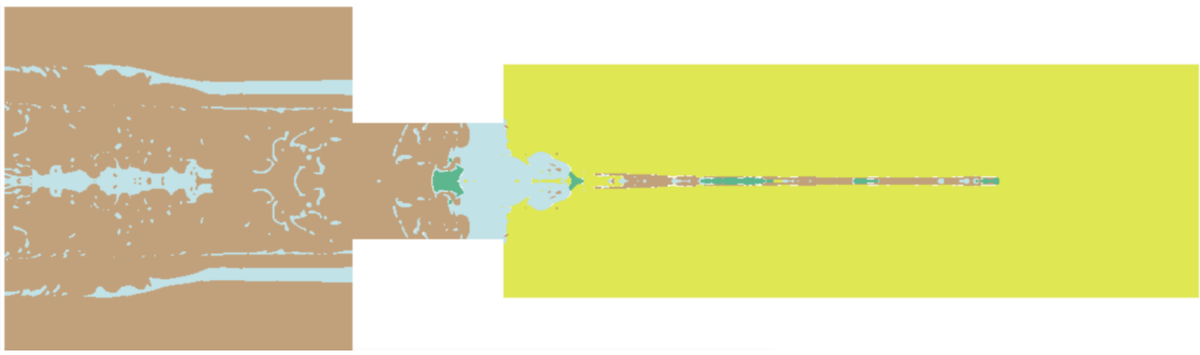

Figure 3.6: Closed back casing, 430 mm penetration.

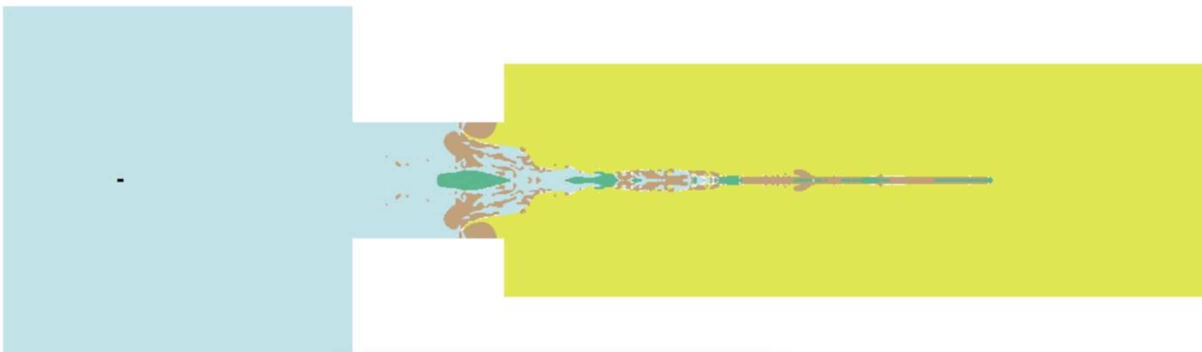

Figure 3.7: Opened back casing, 419 mm penetration.

A comparison between the velocity gradient of both liner jets, at the point of impact with the target, is given by Figures 3.8 and 3.9. It is worth noting that the velocity gradient shown is in m/s. Considering the velocities at the tip of the jet, a 1,19% increase is seen when comparing the closed and opened back geometries. With the difference in both penetrations and velocities not being significant enough and the cost of the closed casing being higher, it was decided to use the open back casing geometry.

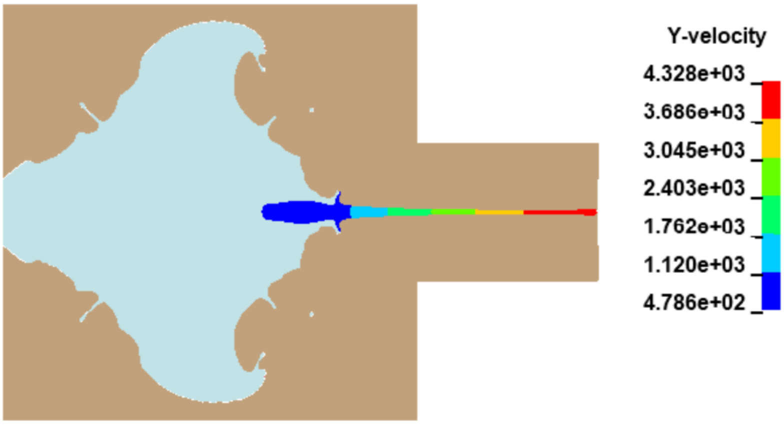

Figure 3.8: Closed back casing jet velocities.

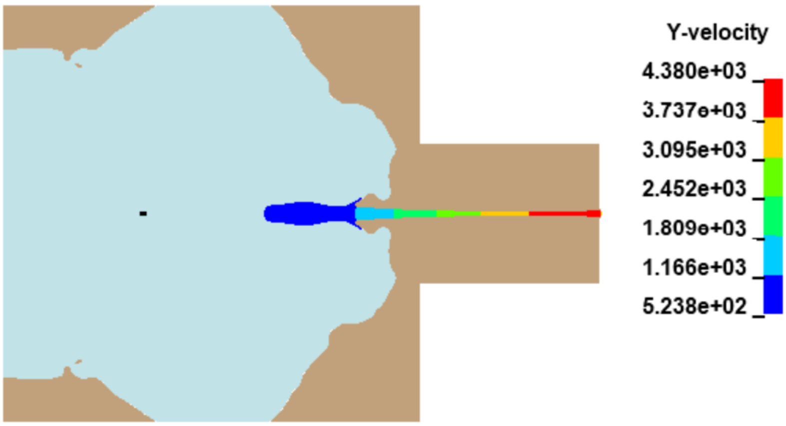

Figure 3.9: Opened back casing jet velocities.

3.3.2 Optimum standoff determination

From the theory already discussed in subsection 2.2.1, there was a need to search for the optimal standoff distance for our geometry. This was achieved by, first, taking in consideration the work of Kulsirikasem et al (2011). As stated previously, for conical charges with copper liner, the optimal standoff was deemed to be 3.63CD. Therefore, taking into account the geometry of the developed shaped charge, an initial standoff distance of 240 mm was considered.

From that initial standoff, the first numerical model was built and then there were iterations varying the standoff distance. A representation of those models and the achieved penetrations on the concrete target can be seen in Figure 3.10, in which the standoff distances are 215 mm, 230 mm and 250 mm respectively.

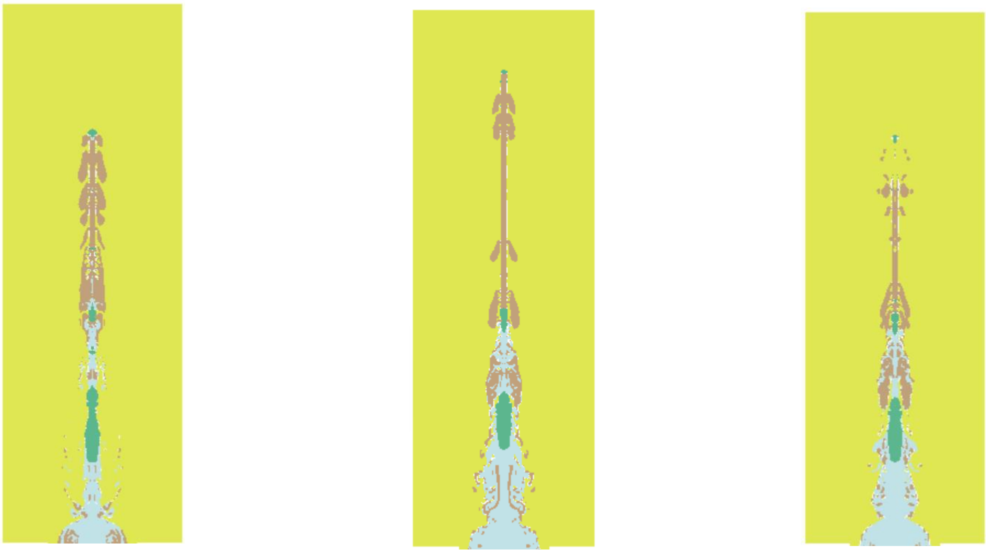

Figure 3.10: Penetration at 215 mm, 230 mm and 250 mm standoff.

Based on the achieved results, 230 mm standoff corresponds to the highest penetration, for that reason it was the design value to be used as the standoff distance for the envisioned shaped charge.

3.4 Numerical model results

As previously referred, numerical models make it possible to obtain information about numerous factors, however, the validation of those results through experimental comparison is challenging. The results taken from the numerical models were mainly focused on determining the expected penetrations for the plain concrete model and the concrete with ceramic spheres. Additionally, jet velocities will also be analysed to better understand the behaviour of the shaped charge and the spheres influence.

3.4.1 Plain concrete

The set of images illustrated in Figure 3.11 characterizes a timeline of the liner collapse for the plain concrete model. The tip of the liner formed due to its collapse can be seen forming at t=0,014 ms, impacting the target at t=0,074 ms. The jet travels cohesively until t=0,15 ms, when it starts to break. Even though it is possible to register further development of the jet, one may observe that there is no significant change in penetration above t=0,7 ms, with the maximum observed penetration of 530 mm.

0 ms

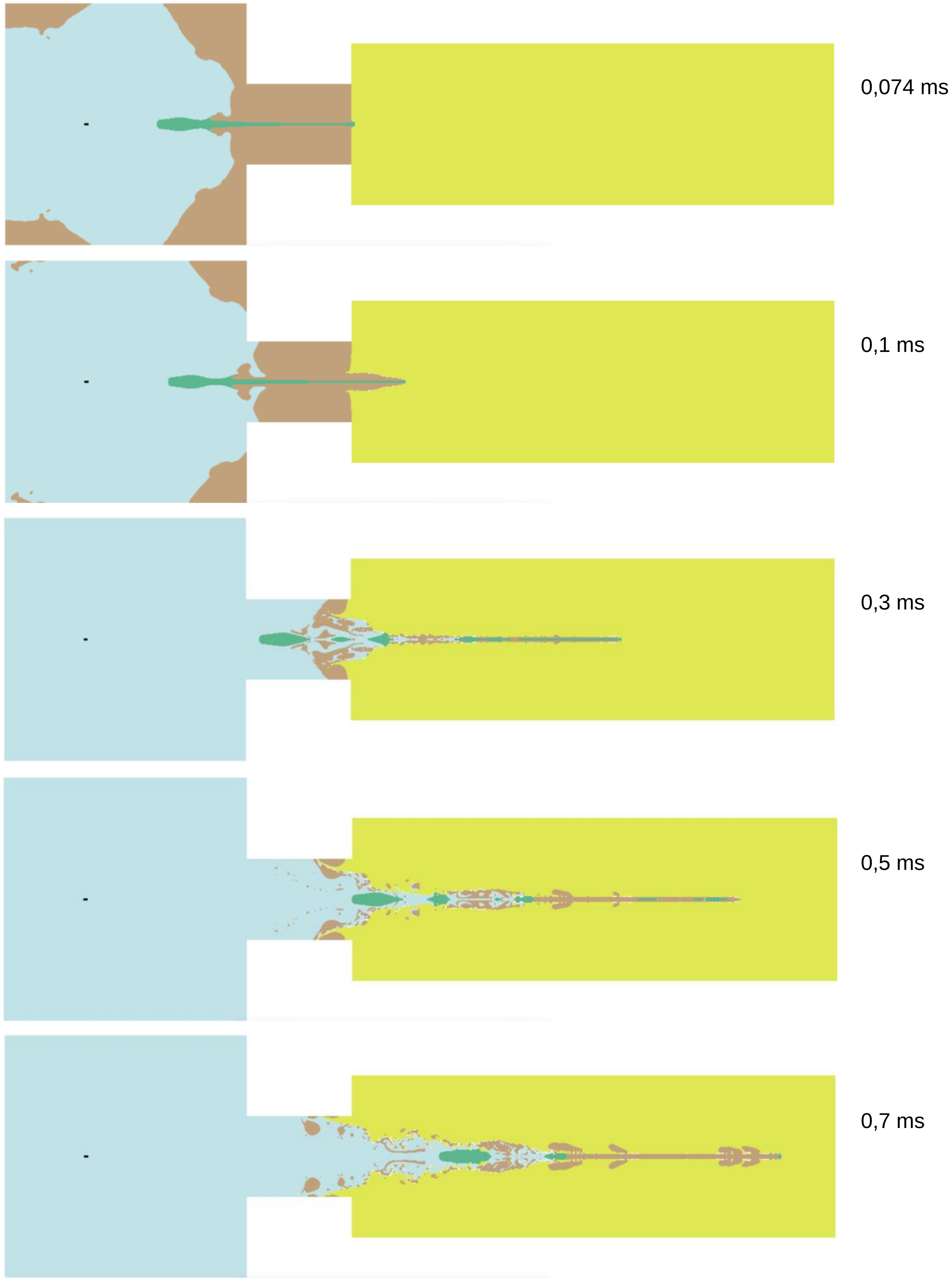

Figure 3.11: Jet development on the plain concrete model.

3.4.2 Concrete with ceramic spheres

The addition of the ceramic spheres poses a challenge for this type of model. The specimens developed for the experimental campaign, reported in Chapter 4, possessed 3 layers of ceramic spheres covering the entire surface close to the top of the target. However, with the elaboration of a 2D

ALE axisymmetric model, this could not be exactly replicated, due to the lack of axisymmetry of the experimental specimen.

To create a sphere in the numerical model, the user must define a semicircle which will then be revolved around the centre axis. Without this element being centred, the revolution of an uncentred circle would result in a torus. Therefore, the following model displays only the centred ceramic spheres, as created and presented in Figure 3.12. This obviously constitutes an approximation; however, the development of a full 3D model was deemed unacceptable due to the prohibitive computational cost when compared with the available resources.

Figure 3.12: Concrete with 2 ceramic spheres FEM.

Figure 3.13 describes the liner collapse for the concrete with ceramic spheres model. It is worth mentioning that the behaviour of the jet is the same as the one visualized with the plain concrete model until the impact with the first ceramic sphere, at t=0,084 ms. The measured penetration at the final stage was 460 mm, reflecting a 13,21% reduction when comparing to the penetration achieved with the plain concrete model.

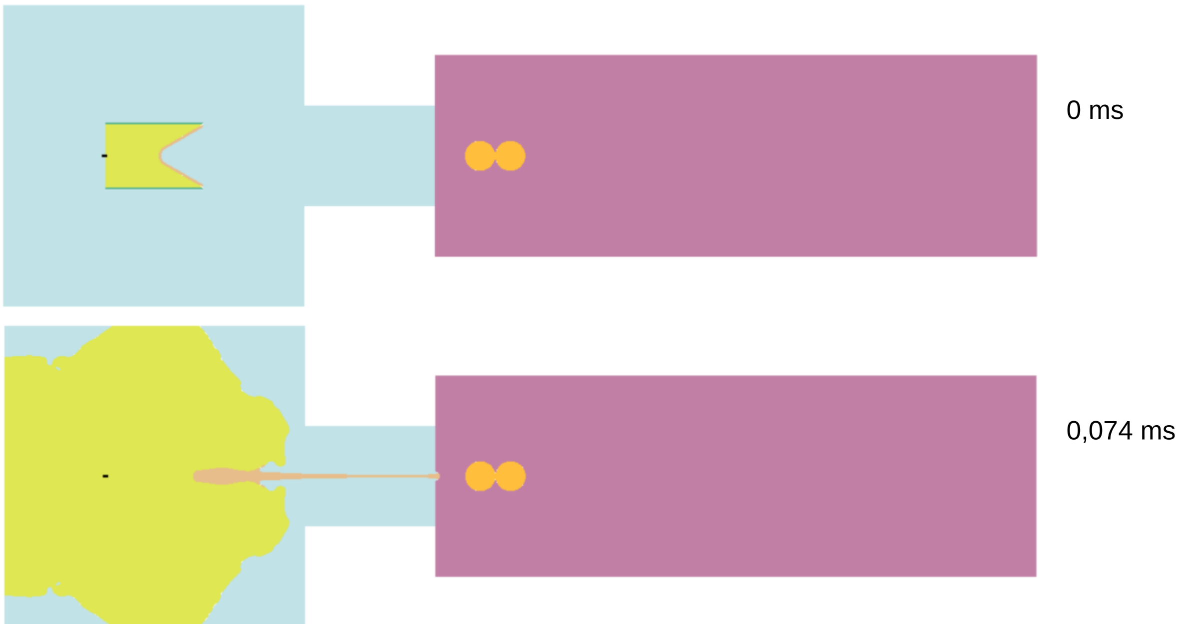

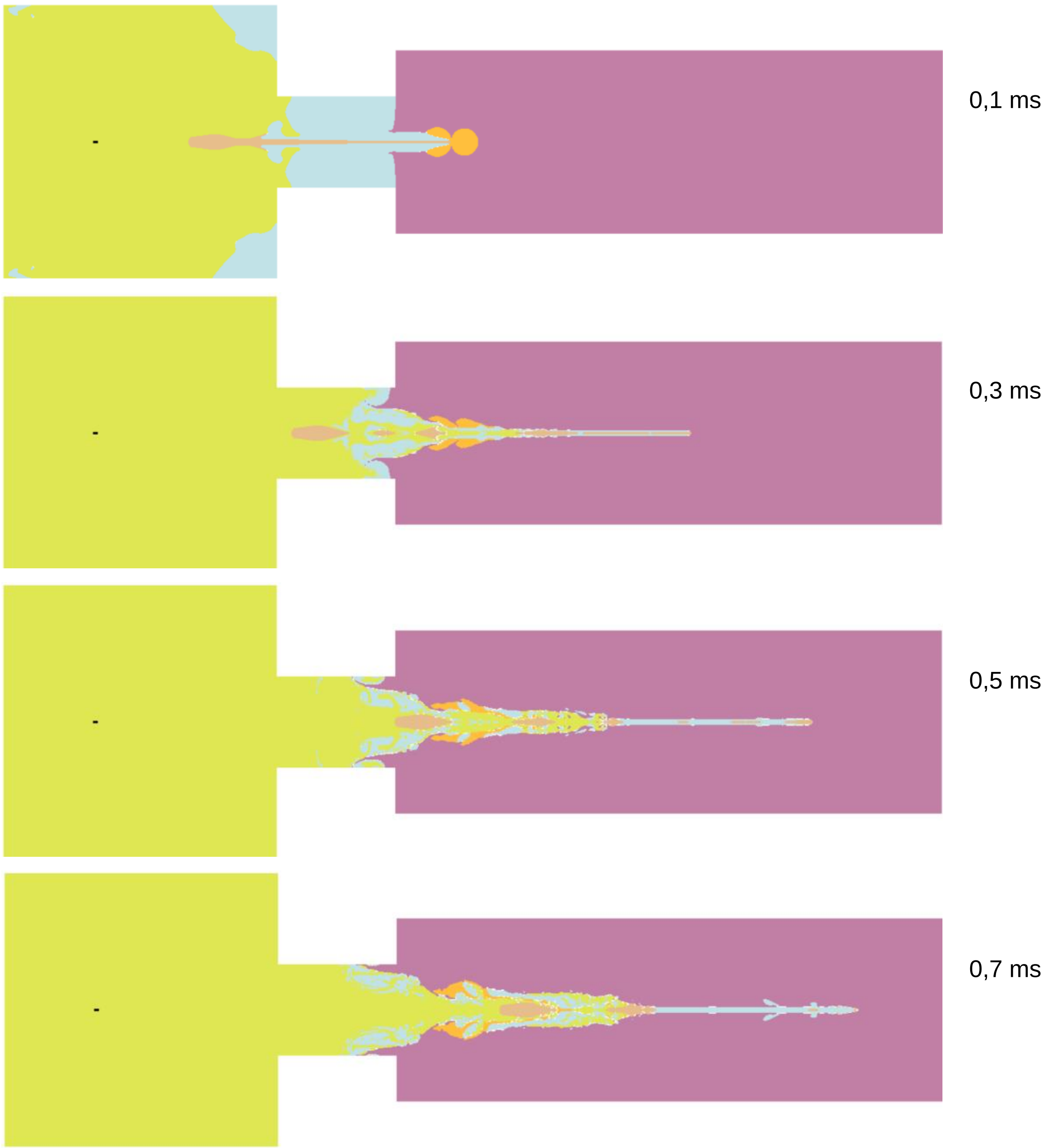

Figure 3.13: Jet development of the concrete with ceramic spheres model.

The influence of the ceramic spheres can also be seen when comparing the jet velocities from the current model with the plain concrete model at the moment it passes through the first and second spheres, t=0,101 ms and t=0,124 ms, as shown in Figures 3.14 and 3.15. Taking the maximum velocities into consideration, a 2,75% decrease can be observed when comparing the velocities of both jets at t=0,101 ms. In addition, a 6,22% reduction is also registered at t=0,124 ms. These slight reductions were to be expected due to the small dimensions of the spheres and their higher density when compared to concrete.

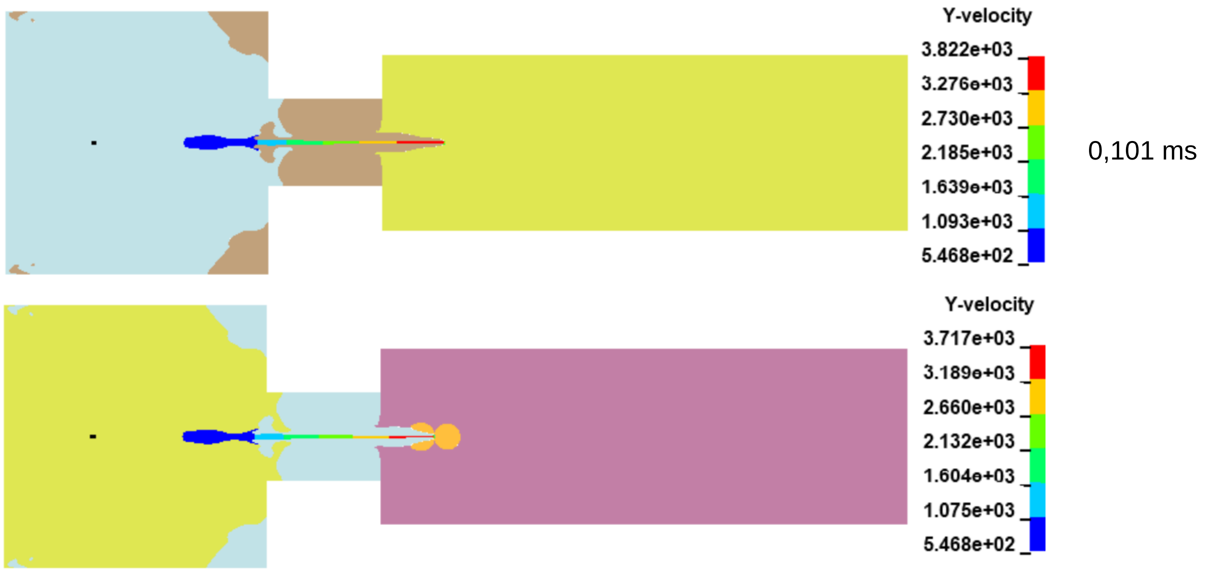

Figure 3.14: Comparing jet velocities at t=0,101 ms.

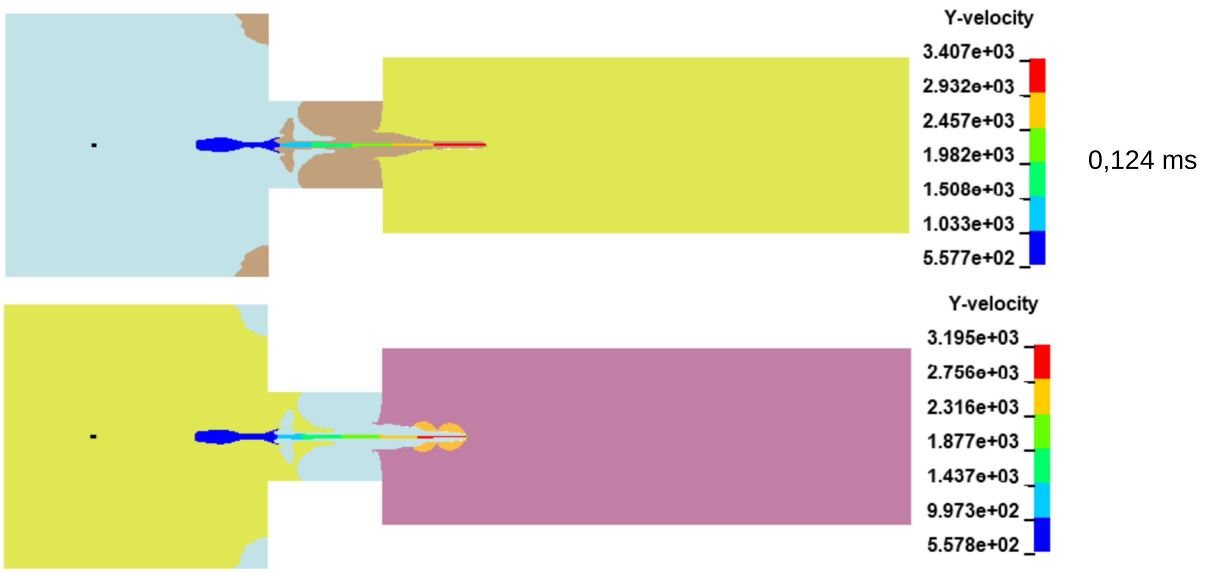

Figure 3.15: Comparing jet velocities at t=0,124 ms.

4. Experimental campaign

For this dissertation, an experimental campaign was carried out at the Santa Margarida military camp with qualified military personnel responsible for the safe handling, transport, and storage of the explosive materials, ensuring full compliance with the safety regulations of the Portuguese Army.

This chapter delineates the construction of the shaped charges and targets, the various experimental tests that were conducted, providing insights into their methodologies and procedures. Subsequently, it delivers the obtained results and offers a thorough analysis and interpretation of these findings.

4.1 Experimental procedures

4.1.1 Shaped charge construction

The copper cone for the liner was created from a solid block of copper being cut according to the specifications from the computer aided design (CAD) model using computer numerical control (CNC) machining techniques. The steel casing was created using sections of a steel tube with 2 mm thickness and an external diameter of 66,8 mm. The copper liners and steel casing may be seen in Figure 4.1.

Figure 4.1: Copper liner and steel casing.

The explosive used to fill the casing was PE4A, a hexogen based plastic explosive. In this process, 350 grams of explosive was used per charge, on average, with it being carefully compacted to prevent voids. Figure 4.2 shows one of the PE4A candles used.

Figure 4.2: PE4A candle.

To have the desired standoff distance, sections with 230 mm of polyvinyl chloride (PVC) tubes with 75 mm in diameter were used. In an attempt to record the jet with high-speed cameras, 2 cuts were made longitudinally in the PVC sections, however, this proved to be an inadequate solution since the velocities of the jet and the debris from the explosion were such that it was not possible to collect useful data. A representation of the used PVC tubes is seen with Figure 4.3.

Figure 4.3: PVC standoff section.

While assembling the different parts and positioning the charge on the centre of the target, an alignment and levelling tool was used to ensure the experimental results would be the closest to the numerical model, as demonstrated by Figure 4.4.

Figure 4.4: Shaped charge alignment.

Table 4.1 displays the mass of each shaped charge component as well as the average, maximum, minimum and standard deviation (SD) mass for each group. It can be observed that the mass of each casing and explosive were consistent withing their respective group, having low deviations. The deviations in total mass are due to the liner components, with this group having considerably higher deviations when comparing to the casing and explosive groups.

Table 4.1: Shaped charge composition masses.

Charge Number	Total Mass [g]	Liner Mass [g]	Casing Mass [g]	Explosive Mass [g]
1	780,20	128,00	302,40	349,80
2	779,80	126,90	302,70	350,20
3	783,90	131,00	302,90	350,00
4	779,50	126,10	303,00	350,40
5	778,70	125,80	302,90	350,00
6	779,50	126,40	303,10	350,00
7	779,40	127,10	302,10	350,20
8	776,30	124,10	302,40	349,80
9	779,60	127,40	302,20	350,00
10	783,80	131,40	302,40	350,00
11	777,50	125,10	302,50	349,90
12	779,70	126,70	303,40	349,60
Average	779,83	127,17	302,67	349,99
Max	783,90	131,40	303,40	350,40
Min	776,30	124,10	302,10	349,60
SD	2,08	2,06	0,38	0,20

4.1.2 Concrete and explosive validation

To make sure the values taken from literature and used for the numerical model were accurately describing the behaviour of the materials available for the experimental campaign, experimental tests were also made. *Betão Liz*, the company that supplied the targets, performed compression tests on the concrete, from which a compressive strength of 42,1 MPa was attained. The full experimental reports may be seen in annex A.

The detonation velocity of the explosive was verified performing an *in-situ* experiment. A stretch of explosive was placed on a surface and 3 electric wires were placed 10 cm apart from each other. This process is depicted in Figure 4.5 and 4.6. The wires were then connected to a commercially available velocity measuring system.

Figure 4.5: Explosive dimensions.

Figure 4.6: Wires connected to explosive.

The achieved velocity was determined to be 6385,70 m/s, which is roughly an 8,8% reduction when comparing to the 7000 m/s given by literature. This reduction was taken into consideration during the improvements made in Chapter 5.

4.1.3 Targets

The envisioned experimental campaign was performed using in total 12 barrels, 4 of each type. Type S barrels are filled with plain concrete and type E barrels are filled with concrete with 3 layers of ceramic spheres that are 30 mm from the top. The ceramic spheres are displayed in Figure 4.7, their properties and dimensions are given Table 4.2.

Figure 4.7: Ceramic sphere.

Table 4.2: Ceramic spheres properties.

	Ceramic spheres
Density	3,65 g/cm^3
Chemical composition	92% Al_2O_3
Diameter	30 mm

Lastly, Type NN barrels have the same composition as type E with the addition of a non-Newtonian fluid to fill the open spaces between spheres. It is important to notice that the addition of the non-Newtonian fluid came as an idea due to the materials availability, offered by *Polyanswer,* and it does not constitute the main focus of this work. This fluid was not taken into consideration during the creation of the numerical models, therefore, its effect on the interaction between liner and target will only be evaluated through the collected experimental data. A full description of the used fluid can be found in annex B.

The fabrication of the different targets is illustrated in Figure 4.8.

Figure 4.8: Targets fabrication process.

A representation of the different targets, with dimensions in mm, is provided. Type S, E and NN are depicted in Figure 4.9 (i), (ii) and (iii), respectively.

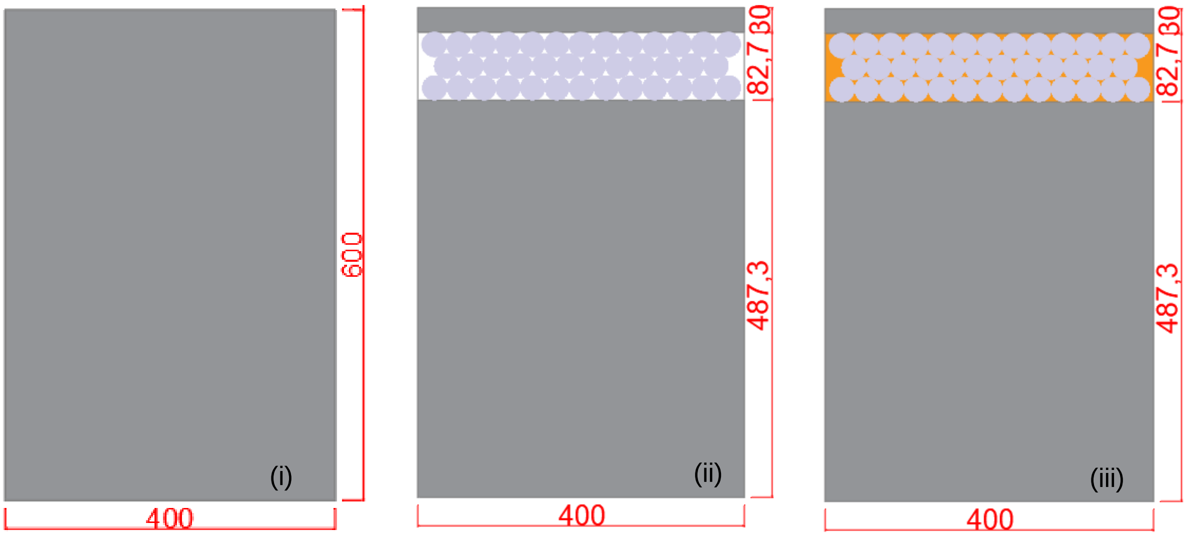

Figure 4.9: Target types.

4.1.4 Experimental setup

The representation of the setup and the actual testing setup can be seen in Figure 4.10 (i) and (ii), respectively.

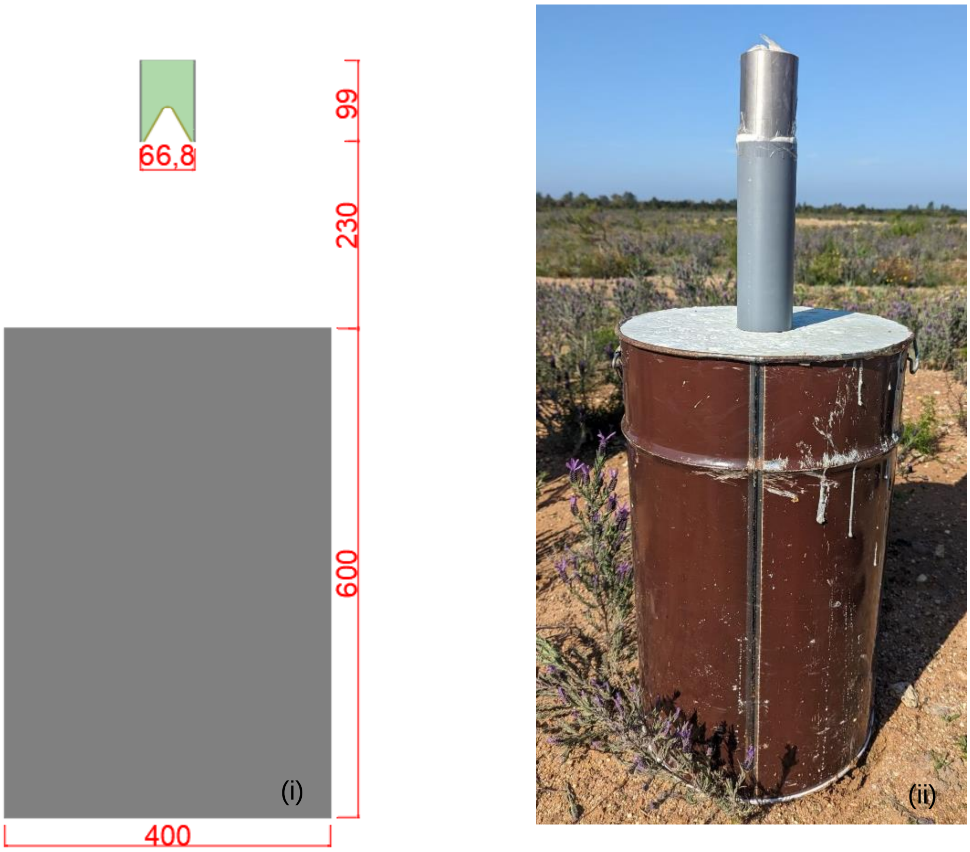

Figure 4.10: Experimental setup.

4.1.5 Measurements procedures

To validate the numerical model, the penetration, affected diameter, entry diameter and volume of the borehole were analysed after the liner's impact. Surface cracking on the target and comparison of the bigger fragments were also examined as a mean to detect different behaviours on the specimens.

The data collection process was as follows:

- **Total penetration** - measured using a metal rod with a 2 mm diameter. The small diameter permitted the rod to go through the debris caused by the shaped charge until solid and cohesive concrete was reached, as illustrated in Figure 4.11. This was the first measurement taken after the blast to ensure the different fragments were the least disturbed;

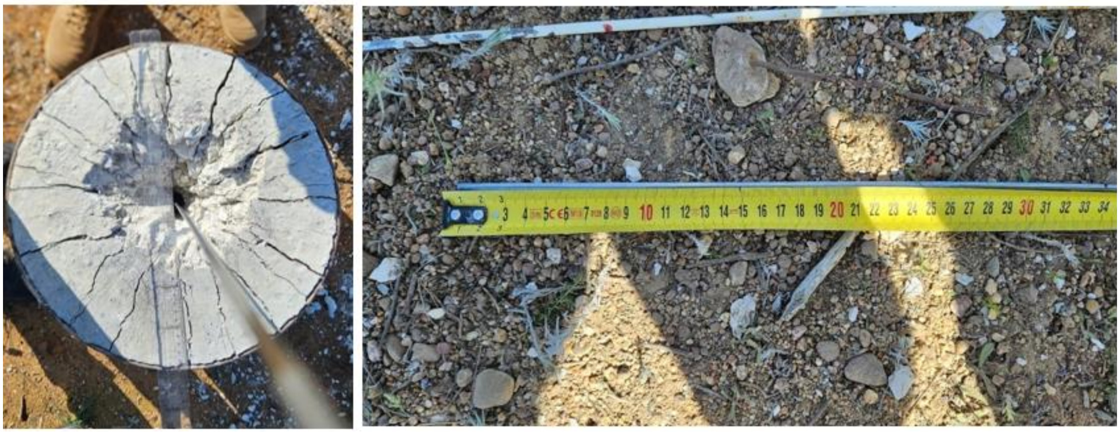

Figure 4.11: Penetration measurement.

- **Affected diameter** – distance with loose debris, established with measuring tape, seen in Figure 4.12;

Figure 4.12: Affected diameter.

- **Entry diameter** – determined with a measuring tape on the top surface of the undisturbed borehole, after taking out the loose debris by hand, see Figure 4.13;

Figure 4.13: Entry diameter.

- **Volume –** to obtain the void space volume, small grain sand was poured to fill this volume, as seen in Figure 4.14. Nonetheless, the results from this procedure should be taken with caution, since taking out the debris may result in a change of the boreholes' dimensions and, therefore, yield an incorrect volume. It should also be considered that the gaps between ceramic spheres will also be filled with sand and that will lead to incorrect measurements for targets E. For NN targets, the fluid fills the hole caused by the shaped charge, so this parameter was not evaluated.

Figure 4.14: Volume measurement.

It should be noted that efforts were made to create a 3D scan of the borehole as well as making a mould of it. This was not successfully achieved.

To support the previous measured perforation and to collect additional information, the decision to cut the targets was made. Firstly, the metal barrel was cut and then the lateral cracked concrete was taken out using a hammer. The above-mentioned process is depicted in Figures 4.15 to 4.17.

Figure 4.15: Barrels being cut.

Figure 4.16: Opened barrel.

Figure 4.17: Penetration measurement on open target.

After opening the concrete, it was also possible to retrieve the liner's remains from inside the target and make a posterior 3D scan of it. From the retrieved liners, data was collected regarding their dimensions, mass and volume. An example of the retrieved liners is provided in Figure 4.18.

Figure 4.18: Recovered liners.

4.2 Experimental Results

4.2.1 S1

Target S1 was impacted by charge nº1. The total penetration recorded after the test was 31 cm, the diameter of the affected area had 15 cm and the entry hole had 4 cm in diameter. The lost volume was 842 ml and the recovered liner weighted 77 g, which represents a 39,8% reduction. See Figure 4.19 and 4.20.

Figure 4.19: S1 impact effects.

Figure 4.20: S1 recovered liner.

4.2.2 S2

Target S2 was impacted by charge nº3. Total penetration recorded with the rod was 34 cm but opening the target proved the liner only penetrated 30 cm. The affected diameter, seen in Figure 4.21, and entry hole were measured at 14 cm and 3 cm, respectively. The lost volume was 853 ml and the recovered liner, Figure 4.22, weighted 78 g representing a 40,5% decrease.

Figure 4.21: S2 impact effects.

Figure 4.22: S2 recovered liner.

4.2.3 S3

Charge nº10 was used on target S3 and its effects are seen in Figure 4.23. Both penetration and affected diameter were recorded at 25 cm while the entry hole was 3,5 cm in diameter. The recovered liner, illustrated in Figure 4.24, weighted 77g which represents a 41,4% reduction. Despite having the lowest overall penetration, target S3 achieved the highest loss in target volume, 1302 ml.

Figure 4.23: S3 impact effects.

Figure 4.24: S3 recovered liner.

4.2.4 S4

Target S4 was impacted by charge nº11, see Figures 4.25 and 4.26. Penetration was first recorded to be 33 cm, but after opening the target, it was discovered to be 46cm. This represented a 39% increase for the total penetration. The affected diameter was registered at 20 cm and the entry hole was 3 cm in diameter. The lost volume was 1072 ml and the recovered liner decreased its mass 38,4%, weighing 77 g.

Figure 4.25: S4 impact effects.

Figure 4.26: S4 recovered liner.

4.2.5 E1

Effects caused on target E1, Figure 4.27, are due to charge nº5. Documented penetration was 32 cm prior opening the target and 29 cm after that. The affected diameter was 12 cm, the entry hole had 3,5 cm in diameter and the lost volume was 727 ml. E1 performed the highest percentual drop in recovered liner mass, 56,3%, with the recovered liner also being the lightest, weighing 55 g and seen in Figure 4.28.

Figure 4.27: E1 impact effects.

Figure 4.28: E1 recovered liner.

4.2.6 E2

Target E2 was impacted by charge nº9, see Figures 4.29. Achieved penetration was 31 cm, with an affected diameter of 13 cm, a 2 cm in diameter entry hole and 612 ml of lost volume. In this case, the liner was not found. Figure 4.30 provides an example of retrieved fragmented spheres.

Figure 4.29: E2 impact effects.

Figure 4.30: Fragmented spheres.

4.2.7 E3

Charge nº4 caused the effects seen on target E3, demonstrated in Figure 4.31.

This target had the highest penetration, noted at 52 cm. However, after opening it, penetration was registered at only 49 cm as shown in Figure 4.32. The registered affected diameter and entry hole were 15 cm and 2,5 cm, respectively, while the lost volume was 842 ml. The recovered liner, illustrated in Figure 4.33, is the heaviest, 84 g, and was registered having the lowest mass reduction, 33,4%.

Figure 4.31: E3 impact effects.

Figure 4.33: E3 recovered liner.

Figure 4.32: Penetration after opening target.

4.2.8 E4

Target E4 was impacted by charge nº7. Total penetration was 39 cm, with a 14 cm affected diameter, see Figure 4.34, and a 2,3 cm entry hole. The lost in volume was the lowest registered value, 410 ml and the recovered liner had a mass of 75,4 g which represents a 40,7% decrease and is seen in Figure 4.35.

Figure 4.34: E4 impact effects.

Figure 4.35: E4 recovered liner.

4.2.9 NN1

Charge nº12 was used with target NN1, see Figure 4.36. Total penetration was 21 cm prior opening and 18 cm afterwards. The diameter of the affected area and entry hole are 12 cm and 2 cm, respectively. The recovered liner, Figure 4.37, had a mass of 71 g, hence a 44% loss.

Figure 4.36: NN1 impact effects.

Figure 4.37: NN1 recovered liner.

4.2.10 NN2

Target NN2 was impacted by charge nº8. Its effects are observed on Figure 4.38. Penetration was first registered at 30 cm before opening, having a slight decrease to 29 cm after. Affected diameter was 18 cm and the entry hole had 2,5 cm in diameter. Like the previous liner, it also had a mass of 71 grams, meaning a 42,8% reduction, and is given in Figure 4.39.

Figure 4.38: NN2 impact effects.

Figure 4.39: NN2 recovered liner.

4.2.11 NN3

Charge nº2 was utilized on target NN3. Figures 4.40 and 4.41 represent its effects and recovered liner. Recorded penetration was 30,5 cm, again with a slight decreased to 29 cm after opening, while the diameter of the affected area and entry hole are 20 cm and 2 cm, respectively. The recovered liner had a 50,4% reduction in its mass, weighing 63 g.

Figure 4.40: NN3 impact effects.

Figure 4.41: NN3 recovered liner.

4.2.12 NN4

Target NN4 was impacted by charge nº6, with its liner not being found, see Figure 4.42. It achieved 30 cm in penetration, with an affected diameter of 13 cm and the entry hole was 4 cm in diameter. Figure 4.44 demonstrates the fluid effects, holding the spheres against gravity.

Figure 4.42: NN4 impact effects.

Figure 4.43: Spheres being held by the fluid.

4.3 Experimental Conclusions

A summary of the experimental data will be shown on the Table 4.3.

Table 4.3: Experimental data.

Barrel	Charge	Penetration [cm]	Entry diameter [cm]	Affected diameter [cm]	Lost volume [ml]	Recovered liner [g]	Liner reduction [%]
S1	1	31,5	4	15	842	77	40
S2	3	30	3	14	853	78	40
S3	10	25	3,5	25	1302	77	41
S4	11	46	3	20	1072	77	38
E1	5	29	3,5	12	727	55	56
E2	9	31	2	13	612	not found	not found
E3	4	49	2,5	15	842	84	33
E4	7	39	2,3	14	410	75,4	41
NN1	12	18	2	12	-	71	44
NN2	8	29	2,5	18	-	71	43
NN3	2	29	2	20	-	63	50
NN4	6	30	4	13	-	not found	not found

It can be observed that the entry diameter is somewhat affected by the different type of targets configuration, with an overall average value of 2,86 cm. Considering the division by types, the S type averages an entry value of 3,38 cm, while E type and NN type both achieved an average entry diameter of 2,6 cm.

For the affected diameter, S type targets averaged 18,5 cm; E type targets had the lowest affected diameters, averaging 13,5 cm, NN type targets had some variations on this parameter, registering an average of 15,75 cm. The overall average value for the affected diameter is 15,92 cm.

The overall recovered liners mass was registered at 72,84 g, with S, E and NN types averaging 77,25; 71,47 and 68,33 grams respectively. There appears to be some consistency when comparing the values from the different test apart from E1 and E3 that have the lowest and highest recorded mass, respectively.

Alternatively, a better perception of the effects caused by the different target types should be achieved when analysing the percentage of the lost liner mass because it takes into consideration the different initial masses of the liners. Once again, some consistency is achieved with the overall losses on liner masses being 43%. S type liners lost on average 40% of their mass, E type lost 43% and NN type lost 46%.

When it comes to penetration, there appears to be some variation in the attained values. This was to be expected because the targets are not homogeneous:

- For S type targets, there is an average of 33,13 cm in penetration. However, S4 introduces a significant variation when comparing to the rest of the tests with a 46 cm penetration;
- E type targets had a 37 cm average penetration, but variations are also observed specially with E3 achieving the highest penetration off all targets, 49 cm, which was not to be expected. By considering E3 as an outlier, the new E type average is 33 cm, similar to the S type;
- NN type targets have the lowest recorded penetration and the lowest average penetration by type with 26,5 cm. The addition of the fluid appears to have a significant impact, reducing the penetration capabilities of the shaped charges.

Considering the overall recorded penetration for each target type and discarding E3, the addition of the spheres decreases penetration by 0,38%, whereas the addition of the non-Newtonian fluid increases penetration resistance by 20%, when comparing to the S type targets.

Experimental penetration will now be compared with both the analytical and numerical models' data. The analytical models that will be used in this comparison will be the Birkhoff 1948 model and the FOI model considering the reduction factor, due to their simplicity. These models were also just compared with the experimental results attained through the use of type S barrel targets. For this comparison, it was assumed that the error would be calculated with equation 4.1:

$$Error = \frac{Experimental - Analytical}{Experimental} \tag{4.1}$$

Table 4.4 provides the values for the above-mentioned comparison.

Table 4.4: Experimental and analytical values comparison.

Barrel	Experimental [cm]	Birkhoff [cm]	Error [%]	FOI [cm]	Error [%]
S1	31,5	53	- 68,25	123,9	-270
S2	30		-76,67		-288
S3	25		-112		-366
S4	46		-15,22		-153

As expected, these models have significant differences when comparing to the experimental data due to the complexity in translating this phenomenon into mathematical equations and the difficulties imposed by the target material. The Birkhoff model yielded an overall 68,03% error and the FOI had a 269% error, which is considered as acceptable, since this model is used for practical applications and has protective intentions.

A similar comparison will now be made between the experimental and FEM values, with results visible in Table 4.5.

Table 4.5: Experimental and FEM values comparison.

Barrel	Experimental [cm]	FEM [cm]	Error [%]	Average Error [%]
S1	31,5	53	- 68,25	-68,03
S2	30		-76,67	
S3	25		-112	
S4	46		-15,22	
E1	29	46	-58,62	-29,71
E2	31		-48,39	
E3	49		6,12	
E4	39		-17,95	

It can be seen that the numerical models are overestimating the penetration values when compared with the experimental data. This conservative behaviour makes sense, since FEM are reproducing an optimal and theoretical state. Once again, E3 can be treated as an outlier. If we discard that value, the average error for the E type targets becomes -41,65%. The magnitude of these errors indicates that there is room for improvement of the numerical models, which is demonstrated on the next chapter.

5. Numerical model improvements

The first modifications performed to improve the model behaviour were on the concrete material parameters. As an alternative to keeping all the automatically generated concrete parameters addressed in subsection 3.2.2, a subsequent improvement was made to the material parameter b_1, that controls compressive damage evolution. Wu & Crawford (2015) provides insight into how to estimate this parameter resorting to the expression defined in equation 5.1, where h represents the characteristic length of the element in millimetres. Given our 1 mm square mesh, b_1 was then changed to 0,8035.

$$b_1 = 0{,}0135h + 0.79 \tag{5.1}$$

The second modification to the initial model, and the one with the biggest influence, was the position of the detonator. The preliminary numerical models assumed that the detonator was at the surface of the explosive, at the rear of the shaped charge. However, due to the lack of support during the experimental tests, the detonator had to be placed 3 cm inside of the explosive. Consequently, the location of explosive's initiation in the numerical model was changed accordingly. A comparison between the pressure wave, when it reaches the liner, for the explosive with the detonator at the rear and inside is illustrated in Figure 5.1 (i) and (ii), respectively.

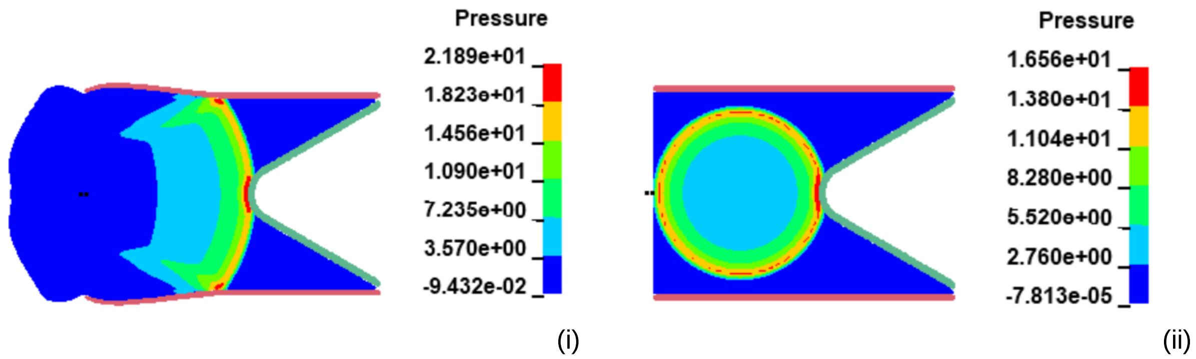

Figure 5.1: Pressure waves reaching the liner.

Table 5.1 reports both the experimental results and the numerical results obtained resorting to the modified numerical model.

Table 5.1: Experimental and improved FEM values comparison.

Barrel	Experimental [cm]	FEM [cm]	Error [%]	Average Error [%]
S1	31,5	39,62	-25,78	-25,61
S2	30		-32,07	
S3	25		-58,48	
S4	46		13,87	
E1	29	36,23	-24,93	-2,16
E2	31		-16,87	
E3	49		26,06	
E4	39		7,1	

With the improvements made, it seems that the experimental results for S4 also achieved a 14% higher penetration than what should be attainable, according to the numerical model. If we consider the FEM as a representation of the best possible scenario and this value is discarded, the error for the S type targets turns into -38,77%

Similarly, the data collected during the experimental campaign shows E4 penetrating 7,1% more than what was expected, according to the new FEM. However, the difference in values from the experimental and numerical analysis was not believed to be significant. By considering E3 an outlier, as stated in the earlier subsection, the averaged error form the ceramic FEM turns into -12%. Taking the new numerical models into consideration, the ceramic spheres introduce an 8,56% reduction in target penetration, which is a significant difference from the 0,38% reported in subsection 4.3.

The reduction in the detonation velocity reported in subsection 4.1.2 was the last improvement made due to only a small portion of the explosive being tested, therefore it is not possible to attest if the behaviour reported is in accordance with the remaining explosive candles used. Therefore, the modifications imposed by this change are shown separately in Table 5.2.

Table 5.2: Detonation velocity reduction influence.

Barrel	Experimental [cm]	FEM [cm]	Error [%]	Average Error [%]
S1	31,5	36,23	-15,02	-14,87
S2	30		-20,77	
S3	25		-44,92	
S4	46		21,24	
E1	29	35,10	-21,03	1,03
E2	31		-13,23	
E3	49		28,37	
E4	39		10,00	

In accordance with the earlier results interpretation, if S4 is discarded, the S model error increases to -26,9% and by deeming E3 an outlier, the ceramic spheres models achieved a -8,09% error. The behaviour of the numerical models with the detonation velocity reduction closer translates the behaviour of the experimental data collected, with the spheres originating a 3,12% reduction in penetration.

6. Conclusions

6.1 Synthesis and main conclusions

This dissertation addressed the concrete behaviour when faced with hypervelocity impacts, an area of study of increased interest, with the objectives of evaluating the protective capabilities of concrete structures with the addition of 3 layers of ceramic spheres. In order to do it, nonlinear numerical models were developed and validated through an experimental campaign. The hypervelocity was achieved by means of a specially designed shaped charge, inspired by the RPG warhead, PG-7VM.

Numerical models are a crucial part of this field of work, enabling multiple iterations and the collection of useful data, once they are validated. For this dissertation, the numerical models were created using a 2D ALE axisymmetric approach, commonly found in literature regarding this field of work mainly due to its reduced computational cost. However, this decision poses a limitation when creating the ceramic spheres.

Preliminary numerical models were used do make a decision regarding the shaped charge geometry, specifically the influence in having an opened or closed back casing, as well as determining the optimal standoff distance. Based on those models, an opened back casing was used due to its lower cost and the difference in both penetrations and velocities not being significant enough, when comparing to the closed casing. The optimal standoff was also determined to be 230 mm.

During the experimental campaign, 3 types of targets were used: S type targets were filled with plain concrete, E targets were filled with concrete with 3 layers of ceramic spheres added and NN targets have the same composition as E targets with the addition of a non-Newtonian fluid, filling the gaps between the spheres.

It was found that the addition of the spheres resulted in decreasing penetration on target by 0,38% and that combining spheres and non-Newtonian fluid caused a 20% reduction in penetration.

Furthermore, it was possible to attest the available analytical penetration models significantly overestimate penetrations, which makes sense considering the difficulties in translating the behaviour of a brittle and non-homogeneous material.

These difficulties are also part of the reason the numerical models are incapable of perfectly describing the experimental results, with the plain concrete model overestimating by 14,87% the experimental penetrations and the concrete with ceramic spheres model overestimating penetration by 8,09%, on average.

This research far outweighs personal goals, it helps to mitigate knowledge gaps within this field of study, hopefully providing useful insights that will make concrete structures more robust when facing hypervelocity threats, making them better suited to deal with extreme events.

6.2 Recommendations for the future

The main goals for this dissertation were achieved, however, there are areas which have room for further development that will be suggested for future works:

- Replicating this study using 3D models to better simulate the real target conditions and behaviour. This would tackle the axisymmetric issue as well as verifying whether the additional computational cost is justifiable or the 2D ALE models are a close and efficient solution;
- Further development of the non-Newtonian fluid applications regarding hypervelocity impacts. This topic was briefly discussed and was not the main subject of the dissertation, however, the experimental results looked promising. The development of numerical models and additional experimental campaigns should be considered.

References

Abedini, M., & Zhang, C. (2021). Performance Assessment of Concrete and Steel Material Models in LS-DYNA for Enhanced Numerical Simulation, A State of the Art Review. Archives of Computational Methods in Engineering, 28(4), 2921–2942. https://doi.org/10.1007/s11831-020-09483-5

Akers, B., & Belmonte, A. (2006). Impact dynamics of a solid sphere falling into a viscoelastic micellar fluid. Journal of Non-Newtonian Fluid Mechanics, 135(2–3), 97–108. https://doi.org/10.1016/j.jnnfm.2006.01.004

Andraskar, N. D., Tiwari, G., & Goel, M. D. (2022). Impact response of ceramic structures - A review. In Ceramics International (Vol. 48, Issue 19, pp. 27262–27279). Elsevier Ltd. https://doi.org/10.1016/j.ceramint.2022.06.313

Ardekani, A. M., Joseph, D. D., Dunn-Rankin, D., & Rangel, R. H. (2009). Particle-wall collision in a viscoelastic fluid. Journal of Fluid Mechanics, 633, 475–483. https://doi.org/10.1017/S0022112009990632

Asenov, S., Lakov, L., & Toncheva, K. (2013). Promising ceramic materials for ballistic protection. In Journal of Chemical Technology and Metallurgy (Vol. 48, Issue 2).

Austin, C. F. (1959). Lined-cavity shaped charges and their use in rock and earth materials.

Ayode Otitoju, T., Ugochukwu Okoye, P., Chen, G., Li, Y., Onyeka Okoye, M., & Li, S. (2020). Advanced ceramic components: Materials, fabrication, and applications. In Journal of Industrial and Engineering Chemistry (Vol. 85, pp. 34–65). Korean Society of Industrial Engineering Chemistry. https://doi.org/10.1016/j.jiec.2020.02.002

Beeman, D. (1978). Shaped Charge - Armor Nemesis.

Birkhoff, G. M. (1948). Explosives with lined cavities. Journal of Applied Physics, 563-582.

Calder, B. (2013). Concrete and Culture: a material history. The Journal of Architecture, 18(5), 744–756. https://doi.org/10.1080/13602365.2013.841352

Candlin, A. (2024). RPG-7: The iconic Soviet weapon used by soldiers, terrorists and militias around the world.

Chen, X. W., & Li, Q. M. (2004). Transition from Nondeformable Projectile Penetration to Semihydrodynamic Penetration. https://doi.org/10.1061/ASCE0733-93992004130:1123

Chou, P., Carleone, J., Flis, W., & Ciccarelli, R. (1981). Improved formulas for velocity, acceleration, and projection angle of explosively driven liners. https://www.researchgate.net/publication/308166958

Cooper, P. W. (1996). Explosives Engineering.

Cronin, D. S., Bui, K., Kaufmann, C., Mcintosh, G., Berstad, T., & Cronin, D. (2003). Implementation and Validation of the Johnson-Holmquist Ceramic M aterial Model in LS-Dyna.

Daudeville, L., & Malécot, Y. (2011). Concrete structures under impact. European Journal of Environmental and Civil Engineering, 15, 101–140. https://doi.org/10.1080/19648189.2011.9695306

de Goede, T. C., de Bruin, K. G., & Bonn, D. (2019). High-velocity impact of solid objects on Non-Newtonian Fluids. Scientific Reports, 9(1). https://doi.org/10.1038/s41598-018-37543-1

Deshpande, A. P., Krishnan, J. M., & Kumar, P. B. S. (2010). Rheology of complex fluids. In Rheology of Complex Fluids. Springer New York. https://doi.org/10.1007/978-1-4419-6494-6

Dhanasekaran, B., Subash, T. R., Engineering Manager, A., Engineering Manager, C., & General Manager, J. (2017). Numerical Modeling of “Concrete Response” to High Strain Rate Loadings.

Downes, D., Bouamoul, A., Nejad Ensan, M., & Baillargeon, Y. (2016). Development of an efficient numerical model for shaped charge analysis. Journal of Defense Modeling and Simulation, 13(3), 355–362. https://doi.org/10.1177/1548512916643768

Dresch, A. B., Venturini, J., Arcaro, S., Montedo, O. R. K., & Bergmann, C. P. (2021). Ballistic ceramics and analysis of their mechanical properties for armour applications: A review. In Ceramics International (Vol. 47, Issue 7, pp. 8743–8761). Elsevier Ltd. https://doi.org/10.1016/j.ceramint.2020.12.095

Elfving, Carl, Karlsson, Svante & Hansson, Håkan: Model for penetration of shaped charges in protective coverings (Modell för penetration av RSV I skyddstäckningar): Swedish Defence Reaserch Agency (FOI), 2005. In Swedish.FOI-R--1680—SE.

Esteban, B., Lenhart, L. M., Rüdiger, L., & Gebbeken, N. (2015). An evaluation of shaped charge experiments using concrete components. International Journal of Protective Structures, 6(3), 439–455. https://doi.org/10.1260/2041-4196.6.3.439

Gonçalves, D. P., De Melo, F. C. L., Klein, A. N., & Al-Qureshi, H. A. (2004). Analysis and investigation of ballistic impact on ceramic/metal composite armour. International Journal of Machine Tools and Manufacture, 44(2–3), 307–316. https://doi.org/10.1016/j.ijmachtools.2003.09.005

Hirsch, E. (1986). Simplified and Extended Gurney Formulas for Imploding Cylinders and Spheres. In Propellants, Explosives, Pyrotechnics (Vol. 11).

Human Needs Exploration: Then and Now Background Information. (n.d.).

Johnson, G. R., & Cook, W. H. (1983). A constitutive model and data for metals subjected to large strains, high strain rates and high temperatures.

Johnson, G. R., & Holmquist, T. J. (2008). An improved computational constitutive model for brittle materials. 981–984. https://doi.org/10.1063/1.46199

Johnsson, F., Vretblad, B., & Sivertun, A. (2012). Shaped charge calculation models for explosive ordnance disposal operations. Journal of Military Studies, 3(1). http://ojs.tsv.fi/index.php/jms/article/view/7699/pdfTermsofuse:http://ojs.tsv.fi/index.php/jms/about/submissions#copyrightNotice

Kennedy, J. E. (1998). The Gurney Model of Explosive Output for Driving Metal.

Kennedy, R. P. (1976). A review of procedures for the analysis and design of concrete structures to resist missile impact effects *. In Nuclear Engineering and Design (Vol. 37).

Kline, H. (1945). The Cavity Charge, Its theory and Applications to the Opening of Explosive Filled Ordnances.

Kulsirikasem W, Julniphitwong A, & Tanapornraweekit G. (2011). Investigation of Materials for Liners of Shaped Charge Warhead and Their Optimum Standoff Distances.

Latif, Q., Rahman, I., & Zaidi, A. (2012). Impact energy of hard projectile from local damage of concrete slab.

Lee, M., & Yoo, Y. H. (2001). Analysis of ceramic/metal armour systems. In International Journal of Impact Engineering (Vol. 25).

Li, Q. M., Reid, S. R., Wen, H. M., & Telford, A. R. (2005). Local impact effects of hard missiles on concrete targets. International Journal of Impact Engineering, 32(1–4), 224–284. https://doi.org/10.1016/j.ijimpeng.2005.04.005

LSTC. (1992). LS-DYNA ® KEYWORD USER'S MANUAL VOLUME II Material Models. www.lstc.com

Madhu, V., Ramanjaneyulu, K., Balakrishna Bhat, T., & Gupta, N. K. (2005). An experimental study of penetration resistance of ceramic armour subjected to projectile impact. International Journal of Impact Engineering, 32(1–4), 337–350. https://doi.org/10.1016/j.ijimpeng.2005.03.004

Malesa, P., Sławiński, G., & Pęcherzewska, K. (2021). Numerical analysis and experimental test for the development of a small shaped charge. Applied Sciences (Switzerland), 11(6). https://doi.org/10.3390/app11062578

McIntosh, G. (2014). Explosive modeling using LS DYNA.

Medvedovski, E. (2010). Ballistic performance of armour ceramics: Influence of design and structure. Part 2. Ceramics International, 36(7), 2117–2127. https://doi.org/10.1016/j.ceramint.2010.05.022

Mehmannavaz, H., Ramezani, A., Nabakhteh, M. A., & Liaghat, G. (2021). A practical review study on shaped charge in the last two decades (2000–2020). International Journal of Protective Structures. https://doi.org/10.1177/20414196211017923

Moghisi A N, M., & Squire, D. P. T. (1981). An experimental investigation of the initial force of impact on a sphere striking a liquid surface. In J. Fluid Me& (Vol. 108).

Moss, E. A., Krassnokutski, A., Skews, B. W., & Paton, R. T. (2011). Highly transient squeeze-film flows. Journal of Fluid Mechanics, 671, 384–398. https://doi.org/10.1017/S0022112010005756

Murphy, M. (1983). Shaped-Charge Penetration in Concrete : A Unified Approach.

Murphy, M. J., Baum, D. W., Clark, D. B., Mcguire, E. M., & Simonson, S. C. (2000). Numerical Simulation of Damage and Fracture in Concrete from Shaped Charge Jets. 6th International Conference on Mechanical and Physical Behavior of Materials under Dynamic Loading, Krakow, Poland, September 25-29, 2000.

Murphy, M. J., Kuklo, R. M., & Committee, T. I. B. (1999). Fundamentals of Shaped Charge Penetration in Concrete. 18th International Symposium on Ballistics, 2(January 1999), 1057–1064.

Naeem, K., Hussain, A., & Abbas, S. (2019). A Review of Shaped Charge Variables for its Optimum Performance. Engineering, Technology & Applied Science Research, 9(6), 4917–4924. https://doi.org/10.48084/etasr.3153

Olovsson, L. (2000). ALE and Fluid-Structure Interaction Capabilities in LS-DYNA.

Pack, D. C., & Evans, M. (1950). Penetration by High-Velocity ('Munroe ') Jets: I.

Pugh, E. M., Eichelberger, R. J., & Rostoker, N. (1952). Theory of Jet Formation by Charges with Lined Conical Cavities*. In JOURNAL OF APPLIED PHYSICS (Vol. 23, Issue 5).

Ranade, R. (2014). Advanced cementitious composite development for resilient and sustainable infrastructure.

Reddy, P. R. S., Savio, S. G., & Madhu, V. (2019). Ceramic Composite Armour for Ballistic Protection. In Handbook of Advanced Ceramics and Composites (pp. 1–46). Springer International Publishing. https://doi.org/10.1007/978-3-319-73255-8_10-1

Resnyansky, A. D., Katselis, G., & Wildegger-Gaissmaier, A. E. (2004). Experimental and Numerical Study of the Shaped Charge Jet Perforation against Concrete Target. 21st International Symposium on Ballistics, CD(July 2004), 1.

Resnyansky, A. D., Weckert, S. A., & Delaney, T. G. (2014). Damage of Concrete Targets by Enhanced Shaped Charges Damage of Concrete Targets by Enhanced Shaped Charges. January 2013.

Resnyansky, A., & Weckert, S. (2009). Response of an ultra high performance concrete to shaped charge jet. Proceedings of the 8th International Conference on Shock and Impact Loads on Structures, February, 529–536.

Rottman, G. L. (2011). The Rocket Propelled Grenade. Osprey.

Schardin, H. (1954). Development of the Shaped Charge.

Schwer, L. E., & Malvar, L. J. (2005). JRI LS-DYNA USER WEEK 2005 Simplified concrete modeling with *MAT_CONCRETE_DAMAGE_REL3.

Shao, R., Wu, C., Su, Y., Liu, Z., Liu, J., Chen, G., & Xu, S. (2019). Experimental and numerical investigations of penetration resistance of ultra-high strength concrete protected with ceramic balls subjected to projectile impact. Ceramics International, 45(6), 7961–7975. https://doi.org/10.1016/j.ceramint.2019.01.110

Shevchenko, V. Y., Dolgin, A. S., Sychov, M. M., Makogon, A. I., & Perevislov, S. N. (2024). A promising diamond-silicon carbide composite for enhanced ceramic armor. Ceramics International.

Signetti, S., & Heine, A. (2022). Transition regime between high-velocity and hypervelocity impact in metals.

Tabatabaei, Z. S., & Volz, J. S. (2012). 2 th International LS-DYNA ® Users Conference A Comparison between Three Different Blast Methods in LS-DYNA ® : LBE, MM-ALE, Coupling of LBE and MM-ALE.

Tate, A. (1967). A theory for the deceleration of long rods after impact*. In J. Me&. Phys. Solids (Vol. 15). Pergamon Prm Ltd.

Tawadrous, R. I., Attia, W. A., & Laissy, M. Y. (2016). Using ceramic plates as shielding for concrete blocks against projectile penetration. HBRC Journal, 12(3), 263–271. https://doi.org/10.1016/j.hbrcj.2014.11.011

Tu, Z., & Lu, Y. (2009). Evaluation of typical concrete material models used in hydrocodes for high dynamic response simulations. International Journal of Impact Engineering, 36(1), 132–146. https://doi.org/10.1016/j.ijimpeng.2007.12.010

Uddin, J., Marston, J. O., & Thoroddsen, S. T. (2012). Squeeze flow of a Carreau fluid during sphere impact. Physics of Fluids, 24(7). https://doi.org/10.1063/1.4736742

Urtiew, P. A., & Hayes, B. (1991). Parametric study of the dynamic JWL-EOS for detonation products

Veltkamp, B., Velikov, K. P., & Bonn, D. (2022). High velocity impact on a thin (non-Newtonian) fluid layer. Journal of Fluid Mechanics, 951. https://doi.org/10.1017/jfm.2022.884

Walters, P., & Zukas, J. (1989). Fundamentals of Sharped Charges (J. & S. Wiley, Ed.). Wiley-Interscience.

Walters, W. P., Flis, W. J., & Chou, P. C. (1988). A survey of shaped-charge jet penetration models. International Journal of Impact Engineering, 7(3), 307–325. https://doi.org/10.1016/0734-743X(88)90032-2

Wang, C., Ma, T., & Ning, J. (2008). Experimental investigation of penetration performance of shaped charge into concrete targets. Acta Mechanica Sinica/Lixue Xuebao, 24(3), 345–349. https://doi.org/10.1007/s10409-008-0160-3

Wang, C., Xu, W., & Chung Kim Yuen, S. (2018). Penetration of shaped charge into layered and spaced concrete targets. International Journal of Impact Engineering, 193–206. https://doi.org/10.1016/j.ijimpeng.2017.10.013

Wu, J., Liu, J., & Du, Y. (2007). Experimental and numerical study on the flight and penetration properties of explosively-formed projectile. International Journal of Impact Engineering, 34(7), 1147–1162. https://doi.org/10.1016/j.ijimpeng.2006.06.007

Wu, Y., & Crawford, J. E. (2015). Numerical Modeling of Concrete Using a Partially Associative Plasticity Model. Journal of Engineering Mechanics, 141(12). https://doi.org/10.1061/(asce)em.1943-7889.0000952

Xiao, Q. qiang, Huang, Z. xiang, Zu, X., Jia, X., Zhu, Q. feng, & Cai, W. (2020). Shaped charge penetration into high- and ultrahigh-strength Steel–Fiber reactive powder concrete targets. Defence Technology, 16(xxxx), 217–224. https://doi.org/10.1016/j.dt.2019.04.013

Xu, W., Wang, C., & Chen, D. (2019). The jet formation and penetration capability of hypervelocity shaped charges. International Journal of Impact Engineering, 132(July), 103337. https://doi.org/10.1016/j.ijimpeng.2019.103337

Xu, W., Wang, C., Yuan, J., & Goh, W. (2020). Penetration of a hypervelocity shaped charge into layered and spaced concrete targets. Journal of the Brazilian Society of Mechanical Sciences and Engineering, 42(2). https://doi.org/10.1007/s40430-020-2179-8

Xue, C. Y., Kong, D. R., & Xu, C. D. (2022). Damage Effects of Shaped Charges on Concrete Piles. Genetics Research, 2022. https://doi.org/10.1155/2022/3158111

Zhang, C., Kalia, R. K., Nakano, A., Vashishta, P., & Branicio, P. S. (2008). Deformation mechanisms and damage in α -alumina under hypervelocity impact loading. Journal of Applied Physics, 103(8). https://doi.org/10.1063/1.2891797

Zhang, Y., Zhang, X., Zhao, W., & Hu, F. (2022). Similarity Law Study of Shaped Charges Penetrating a Concrete Target. Buildings, 12(12), 1–14. https://doi.org/10.3390/buildings12122268

Żochowski, P., Warchoł, R., Miszczak, M., Nita, M., Pankowski, Z., & Bajkowski, M. (2021). Experimental and numerical study on the pg-7vm warhead performance against high-hardness armor steel. Materials, 14(11). https://doi.org/10.3390/ma14113020

Annex

A. Concrete compression test

BETÃO LIZ
GRUPO CIMPOR

ESTUDO DE BETÃO
Projeto PriSAEx
Proteção de infraestruturas Sujeitas a Ações Extremas
Betão C25/30.S4.XC2(P).D22.Cl0,40

Laboratório Central
C. P. PORTELA SINTRA

Composições de Betão por m^3

Data das Amassaduras: 31-01-2024

Tipo de Composição	N.º Amas.	Ligante (kg)	Cimento (kg)	Adição (kg)	Areia F (kg)	AB Filer (kg)	Brita 0 (kg)	Brita 1 (kg)	Brita 2 (kg)	Água (kg)	Plast. (kg)	Super. (kg)	Razão A/L	Adjuvantes Plast.	Adjuvantes Super.
Comp. Nº 3242290	4697	290	230	60	440	420	170	370	510	156	2,32	1,74	0,54	0,8%	0,6%
Comp. Nº 3242290 + NNF		290	230	60	440	420	170	370	510	156	2,32	1,74	0,54	0,8%	0,6%

Amassaduras Laboratoriais de 12 litros

Temperatura Ambiente durante as amassaduras: entre e °C

Tipo de Composição	Aspecto Betão	Temp. Betão	Água Amas.	M.V. B.Fresco	Consistência (mm) Espalha.	Consistência (mm) Abaixa.	Tensão de Rotura (MPa) 24 h	Tensão de Rotura (MPa) 2 dias	Tensão de Rotura (MPa) 7 dias	Tensão de Rotura (MPa) 28 dias	Peso Provetes	Crescimento 2/7	Crescimento 7/28	Manut. Trabalha.	Δ (28 dias)
Comp. Nº 3242290	Bom	18,9		2400	550	210	-	19,9	35,0	42,1	8,140				
Comp. Nº 3242290 + NNF										2,8	7,340				

Cimento: CEM II/A-L 42,5 R - Alhandra - Cimpor
Adição: Filer: Filer Carbo 250 - Carbomin - Pragosa
Areia Natural Fina - Sesimbra - NSS | Areia Britada c/ Filer e Britas de Calcário de Alenquer - Agrepor

Plast.: MasterPozzolith 7012 - MBS
Super.: MasterEase 3530 - MBS
Temperatura Média no Tanque de Cura: 20ºC

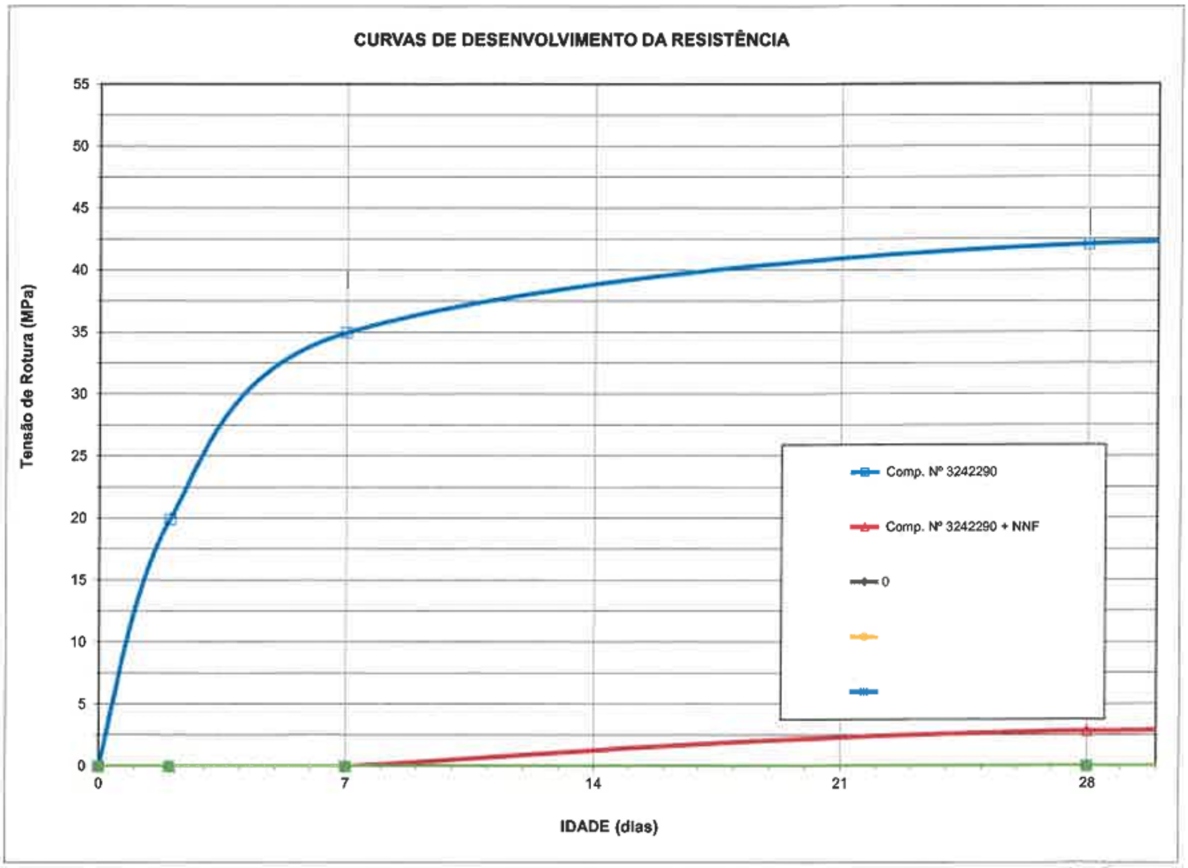

Comentários: o provete com a composição 3242290 + NNF não endureceu após as 24h.

José C. Marques
05-02-2024

BETÃO LIZ

ENSAIOS INDUSTRIAIS

Nº. 4697

Centro de Produção: Porteia de Sintra / Lab Central

Estudo: Proj. de Invest. PriSAEx - Proteção de Infra. Sujeitas a Ações Extremas

Pedido por: Lab. Central

Tipo de betão: C25/30.S4.XC2(P).D22.CL0,40

Cimento: CEM II/A-L 42,5R - CIMPOR - ALHANDRA

Adições: FILLER Carbo 250 - Carbomim - Pragosa

Adjuvantes: Plast: MasterPozzolith 7012 | Super: MasterEase 3530

Outros materiais:

DATA 31 / 01 / 2024

Guia de remessa: P331/BT/139146

Proposta nº: 0100133261

Hora de fabrico: 10:00

Hora da colheita: 10:35

Hora da desmoldagem: 08:50

Volume da amassadura: 2 m^3

Água adicionada: 0 l/m^3

COMPOSIÇÃO UTILIZADA: 3242290

Comp.	Cimento (kg/m^3)	Adições (kg/m^3)	Areia F (kg/m^3)	Areia B (kg/m^3)	Brita 0 (kg/m^3)	Brita 1 (kg/m^3)	Brita 2 (kg/m^3)	Adju. (kg/m^3)	Água (l/m^3)	Obs.
Teor	230	60	440	420	170	370	510	2,32/1,74	156	
Real										

Temperatura (°C)		Tipo de amostra		Aspecto do betão			Abaixamento (mm)	
Ambiente	Betão						Valor	Tipo
15,9	18,9	■ Pontual	☐ Composta	☐ Mau	☐ Razoável	■ Bom	210	■ Verdadeiro ☐ Deformado

Observações:

Cura dos provetes antes de desmoldar: Conforme a NP EN 12390-2: ■ SIM ☐ NÃO

N.º do Molde	N.º do Provete	Data de Ensaio D / M	Idade (dias)	Secção (mm^2)	Massa (kg)	Rotura à Compressão: Força (kN)	Tensão (MPa)	Média (MPa)	Fig. Rotura S	Fig. Rotura NS	Observ.
	1	02/fev	2	22500	8.160	447.4	19.9		x		
	2	07/fev	7	22500	8.140	797.7	35.5	35.0	x		
	3	"	7	22500	8.150	773.4	34.4		x		
	4	28/fev	28	22500	8,130	952,9	42,4		x		
	5	"	28	22500	8,155	942,6	41,9	42,1	x		
	6	"	28	22500	8,140	946,3	42,1		x		
	7	"	28	22500	7,340	63,8	2,8		x		Fluido Polyanswer

Observações:

O Responsável

NORMAS DE REFERÊNCIA: NP EN 12350-1; NP EN 12350-2; NP EN 12390-2; NP EN 12390-3

LAB.04.2

BETÃO LIZ
GRUPO CIMPOR

TRIPLICADO

Guia de Remessa
P331/BT/139146

ATCUD:JFMRT9RB-139146

Local De Carga:
Portela Sintra
Avª Almirante Gago Coutinho, 175
2710 - 901 Sintra
Tel.: 962 723 525
NIF.: 500 045 267
Email: btz.psintra@cimpor.com

CLIENTE
BETÃO LIZ, S.A.
AV JOSE MALHOA 22 PISOS 6 A 11
1099-020 LISBOA

DATA
31-01-2024

CONTRIBUINTE Nº PT500045267 Código A.T.: 15126531712

PROPOSTA Nº	LOCAL DE DESCARGA / IDENTIFICAÇÃO DA OBRA	
0100133261	LABORATÓRIO CENTRAL-PORTELA SINTRA SINTRA - 2710-000	18071254

PRODUTO CONFORME COM:	
NP EN 206	Betão C25/30.S4.XC2(P).D22.Cl0,4

MATERIAIS CONSTITUINTES				VOLUME (m3)	
CIMENTO	ADIÇÃO	ADJUVANTE	OUTRO	PARCIAL	ACUMULADO
---	---	---	---	2,00	2,00

HORA DA AMASSADURA	CONTROLO NA EXPEDIÇÃO		VIATURA		DESCARGA	
	PRODUÇÃO	INSP. VISUAL	Nº	MATRICULA	DIRETA	BOMBA
10:00			3199	AL-89-OV	x	-

HORA DE						MOTORISTA
SAÍDA CENTRAL	CHEG. OBRA	INICIO DESCARGA	FIM DESCARGA	SAÍDA OBRA	CHEG. CENTRAL	
						Pedro Gomes

OBSERVAÇÕES:

Radial: 2

A PEDIDO DO CLIENTE	
ÁGUA ADICIONADA EM OBRA	PROVETES
NÃO ☐ SIM ☐ ___lts	NÃO ☐ SIM ☐ ___un

O Cliente:

Este documento não serve de factura
LZ8e-Processado por programa certificado nº1532/AT
BETÃO LIZ, S.A - Sede: Avenida José Malhoa, 22, Pisos 6 a 11 | 1099-020 LISBOA | PORTUGAL - Tel.: 21 311 81 00 - Fax: 21 356 13 81
NIPC 500 045 267 - Capital Social: 22.000.000.00 EUR - Mat. C. R. C. de Lisboa sob o Nº 500 045 267

CÓDIGO DO PRODUTO	VOLUME (m3)		HORA DA AMASSADURA	Guia de Remessa	
	PARCIAL	ACUMULADO		DATA	Nº
132301412840	2,00	2,00	10:00	31-01-24	P331/BT/139146

Cód. Nome	Humidade (%)	Teórico (kg/m³)	Real (kg/m³)	Desvio (%)
1007Brita 0	0,50	171	167	-2,45
1009Areia B	0,16	421	429	1,94
1010Areia F	9,29	485	484	-0,14
1011Brita 2		510	510	-0,09
1012Brita 1	0,50	372	359	-3,59
AGREGADOS		1958	1948	-0,54

Cód. Nome	Teórico (kg/m³)	Real (kg/m³)	Desvio (%)
2006FILLER	60	61	2,14
2007C42,5 R	230	230	0,17
3006SupPlas	1,59	1,98	24,37
3007MP7012	2,90	2,94	1,38
4001AGUA1			
9999AGUA2	108	109	0,89

CL: BETÃO LIZ, S.A.
Betão C25/30.S4.XC2(P).D22 Cl0,4

OB: 18071254 VT: 3199 Total: 4706 kg
A/L: 0,54

V

B. Non-Newtonian fluid

POLYANSWER

HIGH-IMPACT TECHNOLOGY

Version: 1.6
Revision Date: 13/05/2021

Dilatant Fluid M320

Technical data sheet

Description

The technology patented by Polyanswer provides enhanced protection and flexibility to materials developed for shock absorption and impact protection applications. This dilatant fluid (based on the principle of non-newtonian fluids) can be used as an additive for different materials: foams (polyurethane systems), elastomers and thermoplastic polymers.
To obtain our fluid we use recyclable materials that give excellent impact absorption properties, making products lighter, more flexible, more comfortable, ergonomic, safe, customizable and easy to use.
Its physical form is a viscous paste (natural caramel colour).

Applications

Primarily for individual protection market, such as sports protection or individual protection in work environment. The Fluid can be incorporated into polymeric matrices such as EVA, TPUs and others.

Typical properties

	Value	Unit	Test method
Specific weight	1,21	g/cm³	ISO 1183
Viscosity (40°C)	265	Pa.s	ISO 2555:2018
Impact Test of **10 Joules** at 23°C (transmitted Force in kN)	Sample thickness (mm): 6 – 3,7; 12 – 2,4; 16 – -; 20 – 1,8	kN	EN 20345:2011
Impact Test of **50 Joules** at 23°C (transmitted Force in kN)	Sample thickness (mm): 6 – -; 12 – 6,7; 16 – 6,1; 20 – 5,9	kN	EN 1621-2:2012

Rheological behavior

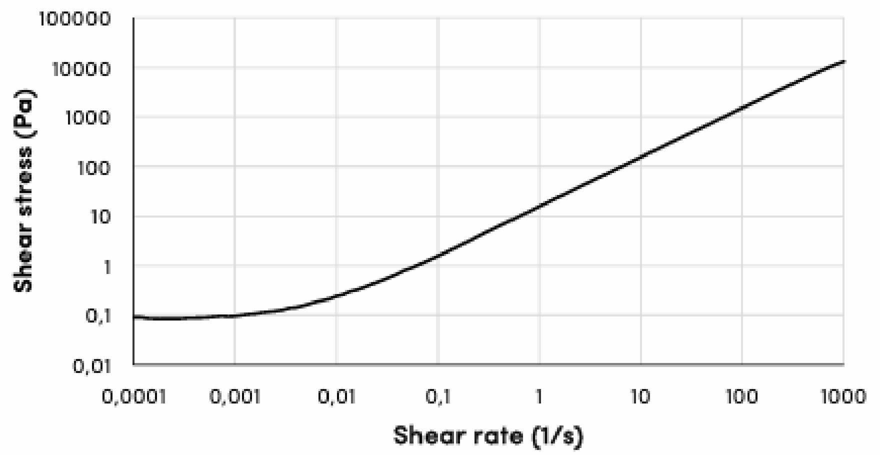

Figure 1 – Shear stress at 40ºC

SpinPark – Centro de Incubação de Base Tecnológica
Zona Industrial da Gandra, S. Cláudio do Barco
4805-017 Guimarães, Portugal

NIPC e Nº Registo Conservatória Comercial de Lisboa:
513140603
Capital Social: €88.095,55

www.polyanswer.com
info@polyanswer.com
+351-253-540-107

How to use

The product is malleable and flexible, but its viscosity increases when a force is applied, so the fluid behaves like a solid, returning to its original flexible state after impact at environment temperature.
It can be used as raw for certain applications or additivated in several materials and formulations such as foams and thermoplastics.
The fluid can be manipulated between 40 and 100ºC of temperature.

Storage conditions

Store the preparation in sealed packaging (avoiding humidity) and away from sunlight. The product must be stored between 10 and 35ºC of temperature.
Shelf life: In these conditions the product is stable for 12 months.

Packaging

Available in 25 kg can or 240 kg drums.
Can be provided kit sample of 2 kg.

SpinPark — Centro de Incubação de Base Tecnológica
Zona Industrial da Gandra, S. Cláudio do Barco
4805-017 Guimarães, Portugal

NIPC e Nº Registo Conservatória Comercial de Lisboa:
513140603
Capital Social: €88.095,55

www.polyanswer.com
info@polyanswer.com
+351-253-540-107